Politecnico di Torino

Master Course in Aerospace Engineering

Master Thesis

Rolling Road Simulations for Drag Coefficient Prediction of Aerodynamic Enablers

Supervisor:

Prof. Gaetano Iuso

Ing. Laura Maria Lorefice

Co-Supervisor:

Prof. Domenic D'Ambrosio

Candidate:

Simone Cesari

March 2018

Contents

List of Figures

List of Tables

Nomenclature

A_f	Car frontal area
C_D	Drag coefficient
C_L	Lift coefficient
F_D	Total drag
F_f	Tangential drag component to surface
F_L	Total lift
F_P	Normal drag component to surface
f	Body force due to gravity
f_R	Friction coefficient
g	Gravity acceleration
M	Car weight
Ma	Mach number
k	Mean turbulent kinetic energy per unit mass
p	Pressure
Re	Reynolds number
$< S_{ij} >$	Mean rate of strain tensor
U	Velocity
U^+	Mean velocity normalized by the friction velocity
u_i	Indicial form for velocity (u, v, w)
x_i	Indicial form for reference axes
y^+	Distance from the wall normalized by the friction length
δ_τ	Friction length
θ	Inclination angle of the road
ρ	Density
ν	Kinematic viscosity $(\nu = \mu/\rho)$

$\nu_t(\overrightarrow{x}, t)$	Turbulent viscosity or eddy viscosity
τ_w	Wall shear stress
CAE	Computer-aided engineering
CFD	Computational Fluid Dynamics
DES	Detached Eddy Simulation
EMEA	Europe, Middle East and Africa
FCA	Fiat Chrysler Automobiles
LES	Large Eddy Simulation
MRF	Moving Reference Frame
MT	Manual transmission
NP	Normal Production
OS	Overset
RANS	Reynolds Averaged Navier-Stokes Equations
SGS	Subgrid-scale
SM	Sliding Mesh
WT	Wind Tunnel

Introduction

In 2016, 15% of CO_2 emission in European Union was due to fuel consumption in the road transportation sector. In cars powered by classical combustion engines, only about 10 % to 40 % of the chemical energy stored in the fuel is available as mechanical energy for the engine. The other part is lost in the form of waste heat because of engine inefficiency. The available energy is consumed by aerodynamic drag, rolling resistance and acceleration [3].

The computational resources available nowadays ensure that automobiles companies have a good correlation between numerical CFD simulations and wind tunnel tests. Compared to wind tunnel tests, CFD simulations are less expansive and allow to study both different models, without the need to change model prototype, and different flow field attributes. However, there are cases, like simulations of rotating wheels, for which the correlation with wind tunnel tests is still under investigation. To investigate this problem different methodologies have been implemented in commercial CFD software which will be presented in this study.

In the study of the flow field around a passenger car an aspect that requires a particular focus is the behavior of the flow field around the wheels. In fact it influences brake cooling, underbody flow, and drag and lift forces acting on the car body. By investigating realistic car models we can find that wheels have a contribute of 30 % to total drag and in particular 2/3 of it is poduced by rear wheels [4]. Figure 1 shows how total drag is distributed, in percentage terms, along the passenger car.

With the above mentioned motivations, the goal of this thesis is the investigation of passenger car drag coefficient, adopting different combinations of aerodynamic enablers, and
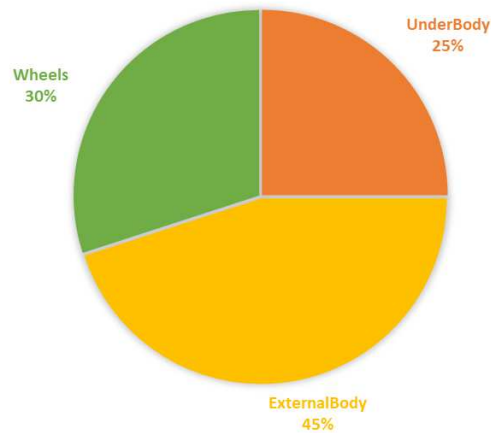
FIGURE 1: Total drag distribution.

the search of methodologies for the rolling road simulations having the best correlation with tunnel tests.

This research has been done at EMEA Product Development Vehicle Concept & Integration - Aerothermal PCC of FCA company located in Orbassano (TO).

STAR-CCM+®commercial code will be used for the numerical simulations while for the pre-processig operation will be used ANSA: an advanced multidisciplinary CAE pre-processing tool that provides all the necessary functionality for full-model build up, from CAD data to ready-to-run solver input file, in a single integrated environment.

In the first step of research, by using *MRF* (Moving Reference Frame) methodology for rotating wheel simulations, the drag coefficient, computed in different cases, will be and compared with the one obtained in wind tunnel tests. *MRF* methodology moves the air into wheel rims by assigning a constant rotation rate and impose a tangential velocity for the physical rotation of the wheel.

Results from previous step allow us to extract case with having high correlation between simulations and wind tunnel tests.

In the second step, the method used to simulate rotating wheel will be changed for those cases having a poor correlation with wind tunnel tests. The method used will be the *Sliding Mesh*, i.e the physical motion of a region around the wheel trim.

In the last step, *Overset* method will be used, i.e the rotation of the wheels mesh (overset region) into ground and car body mesh (background region). This methodology will be implemented in one case only since it requests about 30 days of calculations.

In the cases using *MRF* methodology, RANS turbulence model will be used. Moreover, since there is no physical rotation of the wheel, simulations are stationary. On the other hand in the cases using *Sliding Mesh* and *Overset* methods, DES model will be used. In these cases, since there is a physical rotation of the mesh, simulations are unsteady.

Chapter 1

Automotive Aerodynamics

Interaction between flow and passenger car plays an important role. This interaction is indeed responsible for the forces acting on the vehicle and consequently impacts car emissions and performance.

When we speak of aerodynamics we refer to ventilation, engine in-and-out flows, brake cooling and resulting forces on the vehicle. In particular, for a passenger car, particular attention is put to the drag (i.e. the force acting in the opposit direction of motion) since it causes an increase of fuel consumption and emission. The dependence of the drag on the velocity is shown in Figure 1.1. In particular it can be noticed that such dependence is quadratic [1].

In this chapter, the principal aspects of the interaction of the flow with the car are outlined together with how the flow influence the external aerodynamic of the vehicle.
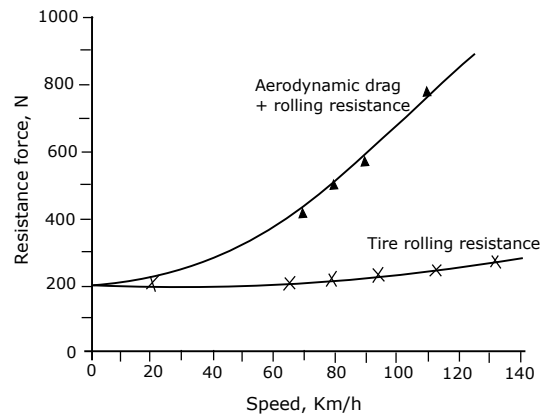
FIGURE 1.1: Total drag as function of velocity.

1.1   Forces on a passenger car

Considering a moving car, the forces acting on it are the *rolling resistance* F_R, the *aerodynamic drag* F_D, the *vehicle mass* M, the *acceleration of gravity* g and the *inclination angle of the road* θ. A schematic representation of all the forces is shown in Figure 1.2.
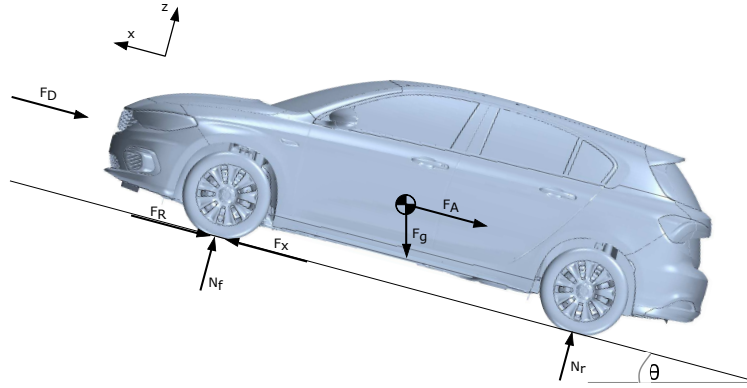
FIGURE 1.2: Forces acting on a passenger car.

At a given instant, the tractive force required is

$$F_x = F_R + F_A + F_G + F_D = f_R M g \cos\theta + M\frac{dU}{dt} + Mg\sin\theta + \frac{1}{2}\rho C_D A_f U^2 \qquad (1.1)$$

If we observe Figure 1.1, we can see that at 60 km/h the dominant term of (1.1) is only the aerodynamic drag F_D. During CFD simulations we can neglect the inclination resistance since it is independent from the velocity. Thus, the only force acting on the car can be attributed to the aerodynamic drag.

The aerodynamic drag is due to the normal (pressure) and tangential (skin friction) component to surface. Hence, we can write the total drag in the follow way

$$F_D = F_P + F_f \qquad (1.2)$$

The drag acting on a car can be determined applying the streamwise momentum equation to a large control volume containing the car since the streamwise trailing vortices is a dominant feature of wakes. These vortices are originated in a different regions of the car and are the drag producers. Now, downstream of the body,the drag can be written in term of three integrals across the fluid stream : the downstream defects in stagnation

pressure and streamwise dynamic head, and the dynamic head of the crossflow velocities in the wake which can be interpreted as a vortex drag[5].

$$F_D = \int \int_A (p_{t,\infty} - p_t)da + \frac{\rho}{2} \int \int_A (U^2 - u^2)da + \frac{\rho}{2} \int \int_A (v^2 + w^2)da \qquad (1.3)$$

where u, v, w are the velocity component in the local system x, y and z in the downstream cross-section and p_t is the total pressure.

In the engineering application a nondimensional number, called the drag coefficient (C_D), is used to quantifies the aerodynamic sleekness of the vehicle configuration.

Thus it is possible to write

$$C_D = \frac{F_D}{0.5\rho U_\infty^2 A_f} \qquad (1.4)$$

Similarly to what was done for drag coefficient, the lift coefficient can be derived from the nondimensionalization of the force acting perpendicularly at drag. Lift is generated from the difference pressure between the top and underneath of the vehicle.

Thus it is possible to write

$$C_L = \frac{F_L}{0.5\rho U_\infty^2 A_f} \qquad (1.5)$$

1.2 Pressure coefficient

An important parameter to quantify how the pressure on a surface deviate from the free stream pressure is the *pressure coefficient C_P*.

$$C_P = \frac{p - p_\infty}{0.5\rho U_\infty^2} \qquad (1.6)$$

If one consider a center section of a car, the flow around it can be considered two dimensional. Now along a streamline external to boundary layer the total pressure is preserved and from the *Bernoulli equation* it can be written

$$p + \frac{\rho}{2}U^2 = p_\infty + \frac{\rho}{2}U_\infty^2 \qquad (1.7)$$
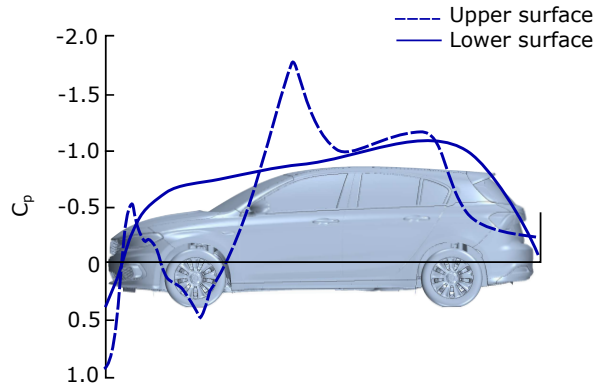
FIGURE 1.3: Pressure coefficient distribution around a generic passenger car.

this leads to

$$C_P = \frac{p - p_\infty}{0.5\rho U_\infty^2} = 1 - \left(\frac{U}{U_\infty}\right)^2 \tag{1.8}$$

where U indicate the external boundary layer velocity.

If one take a middle section of a generic a passenger car, the pressure distribution around this is represented in Figure 1.3. It can be observed that a maximum pressure occurs at the front of the car and this corresponds at the major drag contribution. From this point, with high pressure and low velocity, the flow accelerates rapidly before slowing again with equal rapidity when reaches the windscreen. Because of the slowing air in the windscreen zone, this may not have sufficient momentum to overcome the body surface against the combined resistance of pressure gradient and the viscous frictional forces resulting in separation from the body surface and the creation of a zone of re-circulating flow which is itself associated with energy loss and hence drag. At the aft of the car it can observed an unfavorable pressure gradient and this indicate that a flow separation is likely. The flow separates resulting hence, in pressure drag.

1.3 Ground effect

The ground effect is a phenomena that was investigated in the twentieth century for airplanes takeoff and landing. In fact when an airplane fly very close to the ground it can observed a lift increase.

The same effect can be noted on a car because the streamlines close to the ground are forced to be parallel to the road.

The ground effect is widely used in the race cars to add downforce and only with shape
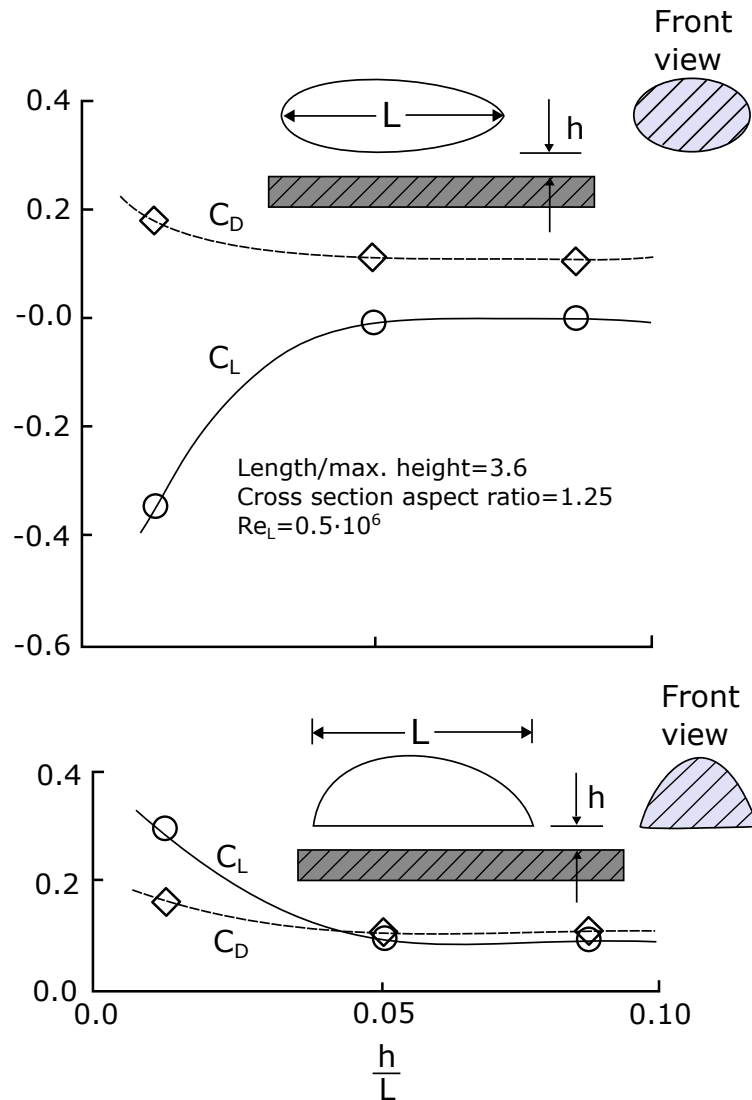
FIGURE 1.4: Ground effect of two generic ellipsoids [1].

modifications is possible to induce downforce.

To investigate the ground effect for a automotive shapes, the two generic bodies represented in Figure 1.4 can be considered. This generic body are an elliptic sections with the same frontal area. The bottom shape in Figure 1.4 is a configuration that tries to block the air flow under the car while the top shape ensures the maximum flow. How it can be noted, both configuration can create low drag coefficients but the latter approach is better if high downforce is required.

When a flow investing a symmetric ellipsoid shape close to the ground, this accelerate under the body and for the Bernoulli's equations this correspond in low pressure and hence more downforce. On the other hand the drag, because of the separation behind the body, increase.

The opposite effect occur when a semi-ellipsoid shape is considered. In fact when this is close to the ground tends to block the flow under the body and, hence, this has lower velocity and higher pressure, corresponding to an increase in lift. The drag, instead, follows a similar trend of symmetric shape body.

1.4 Vortex flow

On a moving car, vortices can grow due to the effect of difference in the flow of local shear, pressure or velocity. The main typical flow fields over generic bodies are shown in Figure 1.5. The main aspect of the creation of this vortices is the formation of two

(A) *Slanted upper surface.*

(B) *"Three box" body.*

(C) *Tapered lower surface.*

(D) *Flow near A pillar.*
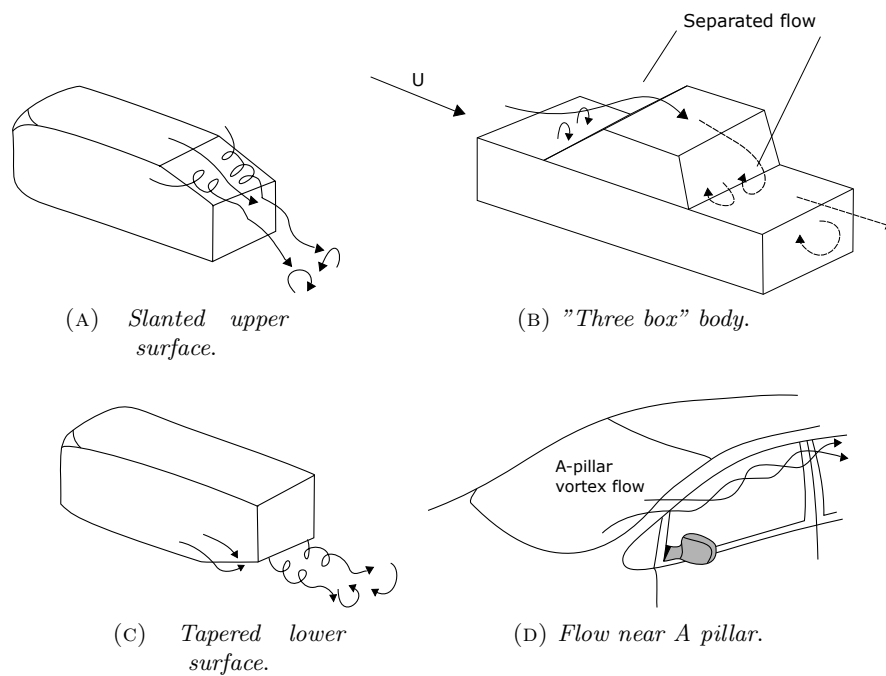
FIGURE 1.5: Vortex flow on generic car shape.

concentrated side edge vortices that influence the nearby flow field. In particular this vortices lead high velocity on the plane and consequently a strong suction forces that induce a lift increase on the surface plane.

Considering the car configuration showed in Figure 1.5(A) in which the rear surface is slanting, for a slant-angle range of $10° - 30°$, it can be noticed the formation of the two vortices previously described. A different typical pattern of flow-separation is what occurring on three-box-body, see Figure 1.5(B), in which it can observed, along the junction between the bonnet and the windshield and between the rear windshield and
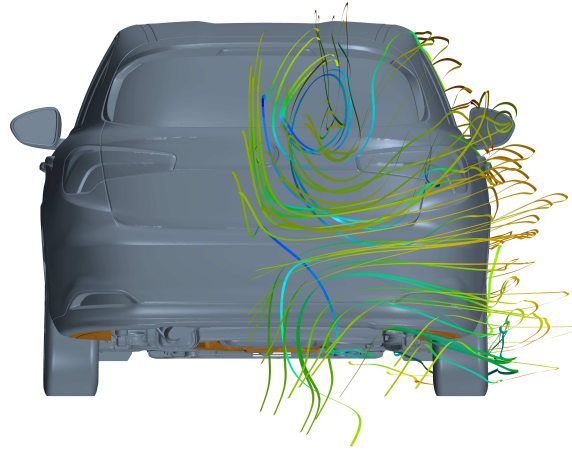
FIGURE 1.6: Wake representation.

trunk area, a creation of a separated bubble with locally recirculating flow.

The configuration showed in Figure 1.5(C) in which is present a slanted surface to lower rear section, is widely used in race car pattern because the two vortices created, generate an increase in downforce.

The last aspect is represented by the vortex generated on the A pillar area, see Figure 1.5(D). In this area the vortex is responsible for water deposition during the motion and the rear view mirror creates an oscillating wake that for high speed causes noise.

The presence of this vortices, created by the separation of the flow, lead to the creation of the wake. In Figure 1.6 it can seen the wake vortex through a streamline representation. In the wake the pressure is lower than the external and, for this reason, the combination of this latter with the higher pressure in front of the car generates an increase in drag resistance.

1.5   Wheel aerodynamics

In the study of car aerodynamic drag, the wheels are responsible for the 25 % of total drag produced.

During the investigation of the flow around a rotating wheel, in presence of the ground, can be seen the creation of three pairs of vortices that are represented in Figure 1.7 [6]. The first pair of vortices leave from the top (3 and 4), the second from the wheel axis (5 and 6) and the third from the bottom (1 and 2). The last pair of vortices, attached to the ground, is called "jetting vortices". In the classical passenger car configuration
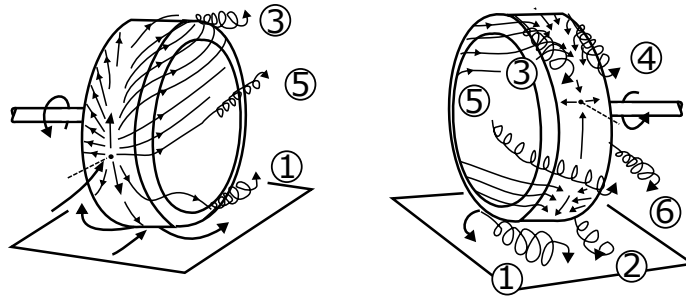
FIGURE 1.7: Vortices around rotating wheel.

is present the wheel arc that is very close to the wheel and allows that three out of this six vortices disappear and only the jetting vortices and external vortex shedding from the wheel axis remain.

In the study carried out by [7] was found that in grooved tyre, due to the Venturi effect, a sudden pressure drop was localized at the contact between wheel and ground, while in case of the slick tyre, in the same place, the pressure reached the maximum. This effect was explained saying that a sudden pressure drop inside grooves promotes the flow through the tread and diminishes the size of trailing vortices.

In the following of this study will be shown how pressure distribution will change if a rotating wheel or a stationary wheel is simulated.

Chapter 2

Numerical Simulations

In this chapter are shown the main mathematical models implemented in commercial CFD software for the study of a flow across a body.

The flow can be described by partial differential equations (*Navier-Stokes equations*) but these cannot be solved analytically except in easy cases. Computational Fluid Dynamics allows to obtain an approximate numerical solution by using a *discretization method* in which differential equations are approximated by a system of algebraic equations. The accuracy of the numerical solution depends on the quality of the dicretizations used [8].

2.1 Numerical methods

The flow across a passenger car is time dependent, three-dimensional, isothermal and incompressible. Assuming a flow velocity running over a car equal to 38 m/s, at sea-level, we can obtain a *Mach number* (Ma) of 0.1. A flow can be considered incompressible when $Ma < 0.3$.

The governing equation for this flow are the continuity equation and the momentum equation (*Navier-Stokes equations*), while the energy equations is neglected.

Navier-Stokes equations in the incompressible and isothermal form can be written as:

$$\frac{\partial u_i}{\partial x_i} = 0 \quad \text{(Continuty equation)} \tag{2.1}$$

$$\frac{\partial u_i}{\partial t} + u_j \frac{\partial u_i}{\partial x_j} = -\frac{1}{\rho}\frac{\partial p}{\partial x_i} + \nu \frac{\partial^2 u_i}{\partial x_j \partial x_j} + \rho f_i \quad \text{(Momentum equation)} \qquad (2.2)$$

In (2.1) and (2.2) tensor notation is used, where $i = (1, 2, 3)$ or (x, y, z), to have a contracted form of equations and f indicate the body gravity force.

Navier-Stokes equations are more complex to solve since they are coupled second order non-linear partial differential equation having an analytic solution only in few cases.

In (2.2) we can notice the different types of transport processes: the second term of left hand side which is a *convective term* and the second term on the right hand side which is a *diffusive term.*

Continuity and momentum equations, however, are not available for turbulence phenomena. In fact, to resolve all turbulent scales, a very large numbers of discretization cells and a huge amount of computational time would be required. It is then necessary to introduce models capable of describing turbulent phenomena.

The next section shows the main models that have been used during this study.

2.2   Reynolds Averaged Navier-Stokes Equation

In a turbulent flow, with boundary conditions and stationary forces, the velocity field is unsteady with oscillations around the temporal average.

As explained in previous section, *Navier-Stokes* equations could describe the motion and every eddies from the largest to the smallest, however the necessary computational resources increase when increasing the Reynolds number ($\sim Re^3$) [9].

Moreover, it should be mentioned that, for most engineering applications, the knowledge of average quantities is enough to solve the related problems.

The most simple equations of this kind are those that govern the mean velocity field. Starting from the decomposition of the velocity $u_i(t)$ into its mean U_i[1] and fluctuations $u_i'(t)$ we can write

$$u_i(t) = U_i + u_i'(t) \qquad (2.3)$$

where

$$U_i = <u_i(t)> = \lim_{T \to \infty} \frac{1}{T} \int_0^T u_i(t)dt \qquad (2.4)$$

---

[1]The average value is considered constant over time.

is the time average of velocity instantaneous values.

All properties can be then splitted into mean and fluctuations part. In the incompressible case the other property is the pressure.

$$p = P + p'$$
(2.5)

Substituting (2.3) and (2.5) into (2.1) and (2.2) and taking the time average of each equation we obtain

$$\frac{\partial U_i}{\partial x_i} = 0 \qquad \frac{\partial u_i'}{\partial x_i} = 0 \quad \text{(Continuity equations)}$$
(2.6)

$$\frac{\partial U_i}{\partial t} + U_j \frac{\partial U_i}{\partial x_j} = -\frac{1}{\rho}\frac{\partial P}{\partial x_i} + \nu \frac{\partial^2 U_i}{\partial x_j \partial x_j} - \frac{\partial <u_i' u_j'>}{\partial x_j} \quad \text{(Reynolds equations)}$$
(2.7)

In (2.7) the term $<u_i' u_j'>$ represent the *Reynolds stresses* that stems from momentum transfer by the fluctuating velocity field.

The *Reynolds stresses* are the component of a second-order tensor with the following properties:

- The diagonal components $<u_i' u_j'>$ are *normal stresses*

- The off-diagonal components are *shear stresses*

- The Reynolds stresses tensor is symmetric, $<u_i' u_j'> = <u_j' u_i'>$

Thus, in appearance, Reynolds equations in (2.7) and *Navier-Stokes* equations in (2.2) are the same, except for the term in the *Reynolds stresses*. The difference between the two equations systems is crucial. In fact in the original system there are 4 equations and 4 unknowns while in the new there are 4 equations and 13 unknowns. This is a manifestation of the *closure problem*.

Consequently, we need additional information to solve the problem. Thus the Reynolds stresses shall be somehow determined [10]

2.2.1 Modelling Turbulence

In order to be able to compute turbulent flows with the RANS equations it is necessary to develop *turbulence models* in order to predict the *Reynolds stresses* and the scalar transport terms allowing to close the system of mean flow equations (2.6) and (2.7). The most common RANS turbulence models are classified on the basis of the number of additional transport equations, see Table 2.1, that need to be solved with the RANS flow equations.

No. of extra transport equations	Name
Zero	Mixing length model
One	Spalart-Allmaras model
Two	$k - \varepsilon$ model
	$k - \omega$ model
Seven	Reynolds stress model

TABLE 2.1: List of turbulence models [2].

This models are based on the *Boussinesq hypothesis* that $< u_i' u_j' >$ terms is a 'diffusive gradient'.

After defining

$$k = \frac{< u_i' u_i' >}{2} \quad \text{(Mean turbulent kinetic energy per unit of mass)} \tag{2.8}$$

we can compute Reynolds stresses exploiting the above mentioned hypothesis:

$$- \rho < u_i' u_j' > + \frac{2}{3} \rho k I = 2\nu_T \left(\frac{\partial U_i}{\partial x_j} + \frac{\partial U_j}{\partial x_i} \right) \equiv 2\rho \nu_T < S_{ij} > \tag{2.9}$$

where $\nu_T(\overrightarrow{x}, t)$ is the *turbulent viscosity or eddy viscosity* and $< S_{ij} >$ is the mean rate of strain tensor.

In the next section is shown the main model that has been used in this study.

2.2.2   The $k - \varepsilon$ model

The $k - \varepsilon$ model belongs to the class of two equations models, in which model transport equations are solved for two turbulence quantities: turbulent kinetic energy k and dissipation rate ε.

From these two equations a length scale can be defined as:

$$l^* \approx k^{3/2}/\varepsilon \qquad (2.10)$$

The turbulent viscosity is then assumed to be

$$\nu_T = C_\mu \frac{k^2}{\varepsilon} \qquad (2.11)$$

where C_μ is one of the five model constants. From experiments $C_\mu = 0.09$ everywhere except near flow boundaries.

The two model transport equations for k and ε are

$$\frac{\partial k}{\partial t} + U_i \frac{\partial k}{\partial x_i} = - <u_i' u_j'> \frac{\partial U_i}{\partial x_j} - \varepsilon - \frac{\partial I_i}{\partial x_i} \qquad (2.12)$$

$$\frac{\partial \varepsilon}{\partial t} + U_i \frac{\partial \varepsilon}{\partial x_i} = C_{\varepsilon_1} \frac{\varepsilon}{k} - C_{\varepsilon_2} \frac{\varepsilon^2}{k} + \frac{\partial}{\partial x_i} \left(\frac{\nu_T}{\sigma_\varepsilon} \frac{\partial \varepsilon}{\partial x_i} \right) \qquad (2.13)$$

where $I_i = -\dfrac{\nu_T}{\sigma_k} \dfrac{\partial k}{\partial x_i}$ and the values of the five constants involved in $k - \varepsilon$ model are obtained by empirical fitting of predictions and experiments. They usually are

$$C_\mu = 0.09, \; C_{\varepsilon_1} = 1.44, \; C_{\varepsilon_2} = 1.92, \; \sigma_k = 1.0, \; \sigma_\varepsilon = 1.3$$

This model can be applied to diverse range of problems such as heat transfer, combustion and multi-phase flows. However the accuracy of this models can be quite low for complex flows. The inaccuracies are due to the turbulent viscosity hypothesis and to the ε equation.

For example modifications to the standard $k - \varepsilon$ model are required in order to apply it to the viscous near-wall region.

This model is widely use in most commercial CFD codes because is computationally

inexpensive when used in conjunction with wall functions.

In presence of separation, boundary layers with adverse pressure gradients, recirculating zones, secondary flows, strong swirl, strong streamline curvature and low Reynolds number this model is notably inaccurate.

In this study has been used a variation of standard $k - \varepsilon$ model: *Realizable Two-Layer $k - \varepsilon$*.

This model contains a new transport equation for the turbulent dissipation rate ε. The coefficient C_μ is expressed as a function of mean flow and turbulence properties, rather than assumed to be constant as in the standard model. Moreover it is combined with the two-layer approach. In two-layer approach the computation is divided into two layers. In the layer next to the wall, the turbulent dissipation rate ε and the turbulent viscosity ν_T are specified as functions of wall distance. The values of ε specified in the near-wall layer are blended smoothly with the values computed from solving the transport equation far from the wall. The equation for the turbulent kinetic energy is solved in the entire flow [11].

2.2.3   Wall function

The presence of a wall causes a number of different effects. Some of them are [10]:

- *Low Reynolds number*: the turbulence Reynolds number $Re_L \equiv \dfrac{k^2}{\varepsilon \nu}$ tends zero as the wall is approached;

- *High shear rate*: the highest mean shear rate $\dfrac{\partial <U>}{\partial y}$ occurs at the wall;

- *Two-components turbulence*: for small y, $<v^2>$ varies as y^4 whereas $<u^2>$ and $<w^2>$ vary as y^2, so that, as the wall is approached, the turbulence tend to the two component limit

- *Wall blocking*: the impermeability condition $V = 0$ at $y = 0$ affects the flow up to an integral scale from the wall.

For these reasons the $k - \varepsilon$ model has to be modified.

Near the wall, in fact, at different distances of this, we can identify three regions in which are prevalent viscous or turbulent effects.

We introduce the following quantities:

- Wall shear stress

$$\tau_w = \rho\nu\frac{dU}{dy}\bigg|_{y=0} \tag{2.14}$$

- Friction velocity

$$u_\tau = \sqrt{\frac{\tau_w}{\rho}} \tag{2.15}$$

- Friction length

$$\delta_\tau = \frac{\nu}{u_\tau} \tag{2.16}$$

From (2.15) and (2.16) we can obtain the dimensionless quantities

$$U^+ = \frac{U}{u_\tau} = U\sqrt{\frac{\rho}{\tau_w}} \tag{2.17}$$

$$y^+ = \frac{y}{\delta_\tau} = \frac{y}{\nu}\sqrt{\frac{\tau_w}{\rho}} \tag{2.18}$$

Now we can identify three regions:

- Viscous sub-layer $(y^+ < 5)$

  In this region, very close to the wall, Reynolds stress are neglected and only the viscous stress dominates.

  We have a linear velocity profile, i.e.:

$$U^+ = y^+ \tag{2.19}$$

- Logarithmic layer $(y^+ > 30)$

  In this region the turbulent shear stress dominates and viscous stresses are neglected.

  We have a logarithmic velocity profile, i.e.:
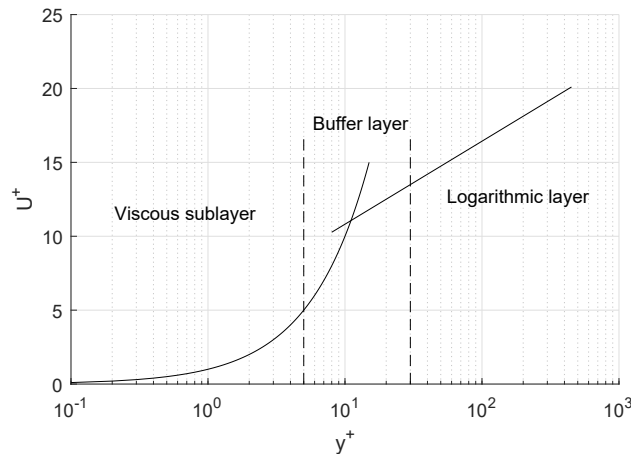
$$U^+ = \frac{1}{k}\log y^+ + C \tag{2.20}$$

FIGURE 2.1: Universal distributions of $U^+(y^+)$ in the wall layer.

where $k = 0.4$ and $C = 5.5$.

- Buffer layer ($5 < y^+ > 30$)

  This is a overlap region between the previous ones, in which both viscous and turbulent shear stresses are relevant.

Figure 2.1 shows the typical mean velocity profile, in a boundary layer, depending on the y coordinate from the wall.

Near the wall the dissipation of turbulent kinetic energy is excessive and it is difficult to capture. Thus, one way is to use a finer grid for turbulence quantities, *near wall approach*, but this is rarely done being computationally heavy. Thus, a modification in $k - \varepsilon$ model is necessary.

In fact, at high Reynolds numbers, the viscous sub-layer is so thin that is difficult to do a fine mesh. This problem can be avoided by using a *wall functions*. Whit this function the center of gravity for the first cell is $30 < y^+ < 300$ (this assume a logarithmic velocity profile for boundary layer) while with near wall approach it is close to $y^+ = 1$.

With wall functions we can apply boundary conditions at a distance that is away from the wall, so that the turbulence model equations are not solved close to the wall. There are two different models of wall function, i.e. *equilibrium wall function*, in which production and dissipation of turbulence are nearly equal, and *non-equilibrium function*. Wall function use the algorithm to resolve the gradients in the boundary layer and for complex geometry the non-equilibrium wall functions is better because the sensitivity for pressure-gradients are higher than for the standard wall functions.

The models previously shown are the classical approaches but in this study a *Two-Layer All y^+ Wall Treatment* was used in which a boundary condition for ε is added.

2.3   Large Eddy Simulation

Another and different approach to simulate turbulent flow is called *large eddy simulation* (LES). Whit this approach only the large scale motions, in inertial range, are simulated because they are much more energetic than the small scale ones. Furthermore, they are the main responsible for the transport of the conserved properties. The large scale motions are simulated with a fine mesh while the smaller scale ones are modeled.

LES application is preferred for flow at high Reynolds number or for complex geometry. Without going into mathematical details, there are four conceptual steps in LES technique:

- The velocity $U(x,t)$ is decomposed into the sum of a filtered component $\overline{U}(x,t)$ and a residual (sub-grid scale) component $u'(x,t)$. $\overline{U}(x,t)$ represents the motion of the large eddies and is three dimensional and time-dependent.

- Definition of the evolution equations of the filtered velocity field, derived from the Navier-Stokes equations. The momentum equation contains the *residual stress tensor* (SGS stress tensor).

- The residual stress tensor is modeled by an eddy-viscosity model to obtain a closure relation.

- The filtered equations are solved numerically for $\overline{U}(x,t)$, which provides an approximation for the large-scale motions.

The same operations can be done for pressure field.

2.4   Detached Eddy Simulation

The Detached Eddy Simulation (DES) approach combines RANS and LES techniques. This model is based on the Spalart-Allmaras one-equation turbulence model. Generally,

in RANS model, length scale d is taken as the distance of the closest point to the wall while in DES it is the minimum between the distance from the wall and a length proportional to the local grid spacing.

Mathematically we can write

$$d_{DES} = min(d, C_{DES}\delta) \tag{2.21}$$

where C_{DES} is a model constant and δ is the local grid spacing. For structured grids, it is the maximum grid spacing over all three directions while for unstructured grid is generally the maximum edge length connecting the centroids of the adjacent cells.

DES turbulence models are set up so that boundary layers and irrotational flow regions are solved using a base RANS closure model. However, the turbulence model is intrinsically modified so that, if the grid is fine enough, it will emulate a basic LES subgrid scale model in detached flow regions. In this way, one gets the best of both worlds: a RANS simulation in the boundary layers and an LES simulation in the unsteady separated regions [11].

2.5   Modelling wheel rotation

When approaching simulations of a rotating body there are different applicable methodologies. Obviously, different approaches will lead to adopting different solutions (steady or unsteady) and, hence, longer or shorter running time.

In this section are described the main methodologies that are implemented in the CFD code and that will be used in this study.

2.5.1   Moving Reference Frame

The simplest approach for modeling a rotating wheel is that of *Moving Reference Frame* in which we impose that the reference frame can rotate with respect to the laboratory reference frame. In this model the mesh is rigid and a steady-state simulation is possible. The purpose of this model is to hold the wheel and to move only the air within the rim. Another consideration in the application of this model is that the moving reference frame give physically realistic results only if the flow in the surrounding volume is axisymmetric

and, hence, no perpendicular velocity component to axis rotation is present [11].

The main required steps to define a rotating condition for the wheel are the following:

- Defining a local coordinate system around which the wheel is rotating;

- Assigning a tangential velocity to the wheel;

- Creation of an interface region and assignment, in the local coordinate system, of a constant angular velocity.

2.5.2   Sliding Mesh

A second approach that we can use to simulate a rotating wheel is the *Sliding Mesh.* This methodology is used when the time-accurate behaviour is required. In fact for this type of approach, an unsteady-state simulation is needed. The CFD code, for the application of this model, provides the option to move mesh vertices of a region [11]. The main guidelines in the model setup are:

- Conformal meshes are preferred, one may use either trimmed cell or polyhedral meshes.
  For polyhedral meshes, the mesh is conformal across the interface because all region can use the same mesh continuum while for trimmed cell mesh it is not possible and each region must have its own mesh continuum and, hence, the mesh in not conformal;

- A region for the moving entities must be created;

- The mesh motion is imposed by the specification of a rotation motion or a rotation and translation motion in the configuration panel of CFD codes.

2.5.3   Overset Meshes

The third and last approach is the *Overset Meshes* or overlapping meshes. This model allows to discretize a computational domain with different meshes that overlap each other in an arbitrary manner.

In the setting of overset meshes, two regions are present: a background region that

enclose the entire solution domain and a overset region that enclose the entities within the domain. In Figure 2.2 is shown a schematically representation of a domain division.
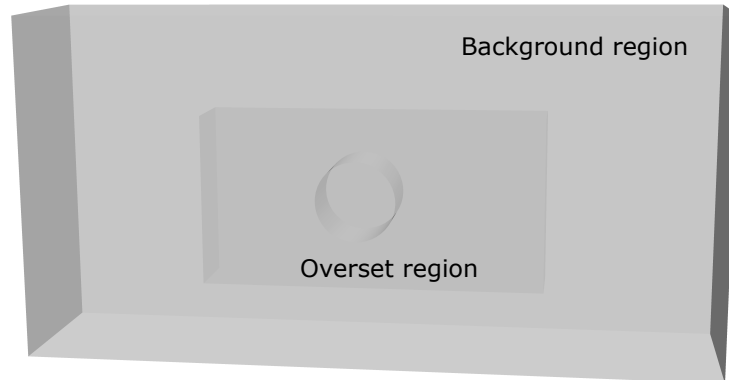

FIGURE 2.2: Domain division for Overset Meshes model.

Once background and overset regions are define, cells are grouped into active, inactive or acceptor cells. Active cells are those where the governing equations are solved while in inactive cells no equations are solved. However inactive cells can became active when the overset region is moving. At the boundary, between active and inactive cells, in the background region, there are the acceptor cells. The latter, in the overset region, are attached to the overset boundary. Acceptor cells, hence, couples solutions on the overlapping grids.

The main guidelines for overset meshes setup are the follow:
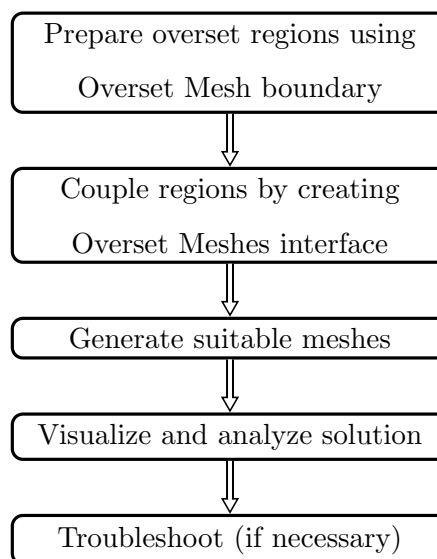
To couple the overset regions with the background region is necessary to create an interface. The interface must be created between each set of overlapping overset regions. There are two options for creating the interfaces:

- Overset Mesh Interfaces;

- Overset Mesh Zero Gap Interfaces.

In this study, zero gap interfaces will be used because of the contact between the tyre and the ground.

When in the CFD codes we establish a zero gap interface between the overset and the background region, automatically a zero gap wall is created in each of the regions. When simulation is running, if overset assembly process detected that the distance between the two zero gap wall boundaries of both region is less than two cell layers, the cells in the gap became inactive. Cell faces between active and inactive cells are placed within the zero gap wall boundaries [11].

Chapter 3

Case Description

The purpose of this study is to investigate aerodynamics drag around a passenger car adopting different methodologies in the simulation of wheel rotation. In particular the goal is to find which method results in the best correlation with wind tunnel tests. For this reason, different configurations of aerodynamic enablers are simulated and the ΔC_D between the Normal Production Configuration (NP) and the new configuration is compared with wind tunnel tests ones.

The passenger car used in this study is the FIAT TIPO 1.6 MJT shown in Figure 3.1 in its NP configuration. NP configuration is equipped with a textile engine shield and a manual transmission (MT).

FIGURE 3.1: Fiat Tipo 1.6 MJT.

In this chapter is described how the different models for rotating wheels simulations have been developed and implemented in CFD codes. Main setting, such as meshes parameters and boundary conditions, are also reported. The ANSA pre-processor software, from BETA company, was used in the pre-processing analysis for CAD model preparation and surface mesh. STAR-CCM+®software, from SIEMENS company, was used for fluid dynamics simulations.

3.1 Aerodynamics Enablers

In order to correlate CFD results with wind tunnel ones, configurations with different combinations of aerodynamics enablers were simulated.

The employed aerodynamic enablers are:

- Front Air DAM, see Figure 3.2(A);

- Front wheel spats, see Figure 3.2(A);

- Engine shield, see Figure 3.2(B);

- Air curtain, see Figure 3.2(A).

(A) *Air curtain, front air DAM and wheel spats.*
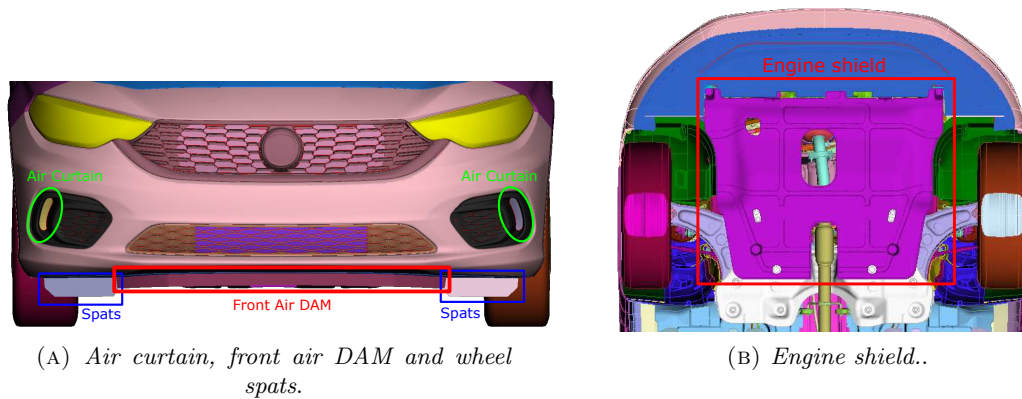
(B) *Engine shield..*

FIGURE 3.2: Aerodynamic enablers.

Aerodynamic enablers have been introduced with the aim to improve the drag coefficient. For example, the introduction of the front air DAM ensures a decrease in the amount of air going underneath, leading to a reduction of drag and an increasing in car stability.
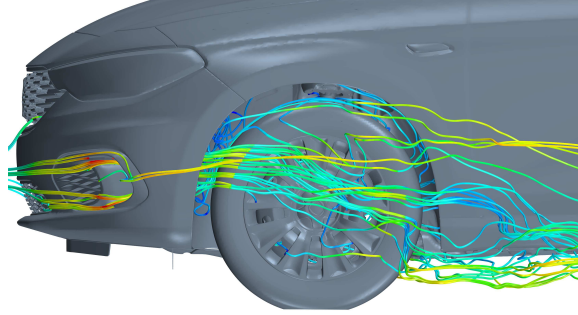
FIGURE 3.3: Air curtains effect.

The air curtains, direct the air stream along the front wheel housing. The accelerated air stream forms a "curtain" and reduces the braking effect of turbulence. Resulting effect is shown in Figure 3.3 with a streamline representation.

Simulated car configurations are summarised in Table 3.1. For each configuration, different models for wheel rotation were used.

Case	Description
001	Normal Production (NP)
002	NP with air curtains closed
003	NP without front air DAM
004	NP without front wheel spats
005	NP without front air DAM and engine shield
006	NP without wheel trims

TABLE 3.1: Simulation case description.

3.2 Computational grid

The first step for a numerical simulation is the creation of a computational grid, i.e. a discretized representation of the computational domain used by physics solvers to provide a numerical solution. The computational domain is a box around the car that represents the test chamber of wind tunnel. The size is designed to lead to a free flow and to neglect blockage of this.

The available computational resources have enabled us to design a box with size $65x40x20hm$. Car was placed at a distance of five times the vehicle lengths from inlet side and eight times the vehicle lengths from outlet side. Cross section height is around thirteen times the vehicle height while cross section width is around twenty times the vehicle width. A representation of the computational domain is shown in Figure 3.4.
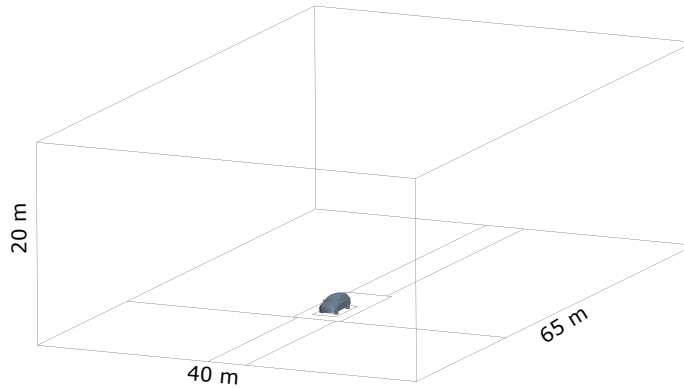
FIGURE 3.4: The domain representation.

Once the domain has been created the next step is the mesh generation. To this aim, vehicle surface mesh and domain were generated through the pre-processor software ANSA. Afterwards, STAR-CCM+®software was used for the fluid dynamics analysis. Last step is the generation of volume mesh, over which physical solvers estimates physical quantities.

The CFD code STAR-CCM+®provides three types of volume mesher: trimmed, polyhedral and tetrahedral mesher, that can be choose according to the strategy of the case. In our cases the trimmed mesher has been used because it provides a robust and efficient method of producing a hight quality grid for both simple and complex mesh generation problems. The trimmer meshing model utilizes a template mesh that is constructed from hexahedral cells from which it cuts or trims the core mesh using the starting input surface. The template mesh contains refinement that is based on the local surface mesh size and local refinement controls.

Together with volume mesher is present a Prism Layer mesher that provides the creation of orthogonal prismatic cell next to wall surface or boundaries. This layer of cells is necessary to improve the accuracy of the flow solution near wall. In fact near wall the determination of forces, heat transfer, flow features such as separation is difficult to predict. The accuracy of flow features depend on resolving velocity and temperature gradients normal to the wall, in fact this are steeper in the viscous sublayer of a turbulent boundary layer and with a coarse mesh the solver is unable to compute the solution near the wall. The use of prism layer, hence, allow to resolve the viscous sublayer directly if the turbulent model supports it (low $y+ \sim 1$). For coarse meshes it allows the code to fit a wall function more accurately (high $y+ > 30$).
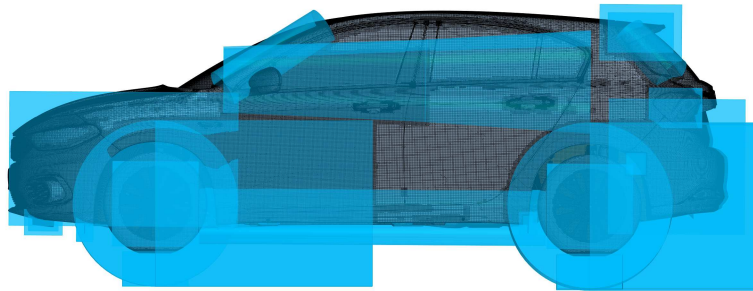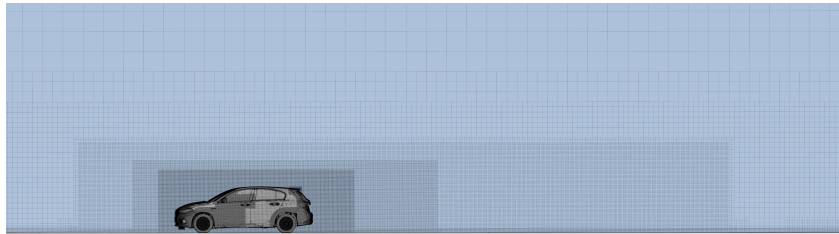
(A) *Volumes refinement representation.*

(B) *Mesh refinement representation.*

FIGURE 3.5: Refinement areas.

Before to run the meshers we need to create refinement volumes in those zone of the vehicle in which is necessary to capture the turbulent and transient flow conditions.

In particular, the areas of greater interest in which the refinement has relevance are:

- Wake zone behind the car;

- Wake zones generated from side mirrors;

- Wake zones generated from the wheels;

- Pillar zones;

- Other zones in which is necessary a better representation of flow features.

In Figure 3.5 are highlighted the areas in which the refinement volumes have been used. In Table 3.2 are shown the main parameters used to set the surface and volume mesh. In the table, base size parameter is indicated with X since it cannot be disseminated. Other parameter, more detailed for single case, will be described in next sections.

Trimmed Cell Mesher					
Parameters	*Standard Value*	*Ground*	*Bumpers*	*Interface*	*Wind Tunnel*
Base Size	$X\ [m]$				
Target Surface size *	100%	100%	50%	PV	100%
Minimum Surface size *	50%	50%	50%	PV	50%
Number of Prism Layer	10	8	PV#	Disable	Disable
Prism Layer Near Wall Thickness *	0.5%	10%			
Prism Layer Near Total Thickness *	80%	160%			

* Values relative to base
#PV=Parent Values

TABLE 3.2: Trimmed cell Mesher parameters.

3.3   Moving Reference Frame

In this section is shown one of the three model used to simulate the rotation of the wheel, i.e. the MRF. As already explained in section 2.5.1 a stationary model is possible because there is not really a rotation of the wheel but only the air into the rim is moved.

3.3.1   Model Preparation

The first step, in the fluid dynamic simulations ,is the model preparation. The pre-processor CAE software ANSA has been used.
For this model, is required the creation of "interface" surfaces between the rim spokes in which the physical quantities are computed. To this surfaces were assigned a constant rotation rate in a local reference frame. Surfaces are shown in fig.3.6.

   The wheel is then put in contact with the ground by enforcing the tyre to have a crushing of 15 mm at the contact with the ground. In this way we can simulate the contact zone between tyres and ground.

3.3.2   Boundary Conditions

In this section a short description of the boundary conditions are presented in order to give an overview of the driving conditions during the simulation (see Table 3.3). To assign a rotation rate at the interface surfaces a local reference frame for every wheel has been created and a stationary motion has been imposed.

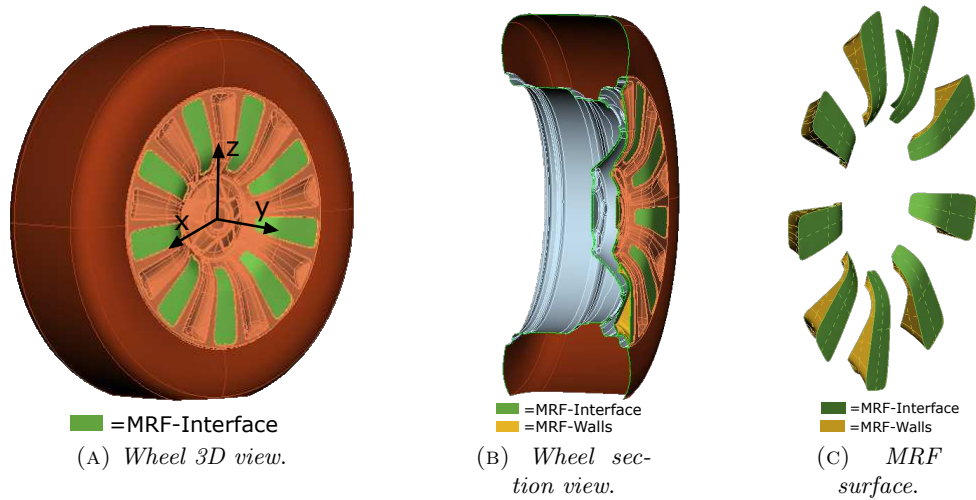   To set the wind speed we assume as reference the one used during wind tunnel tests

(A) *Wheel 3D view.*

(B) *Wheel section view.*

(C) *MRF surface.*

FIGURE 3.6: Wheel for MRF methodology.

Surface	Movement	Type	Condition
Tunnel-wall	Stationary	Wall	Slip
Tunnel-ground	Constant x-velocity	Wall	No-slip Velocity: 38.89 $[m/s]$
Tunnel-inlet	Stationary	Velocity-inlet	0° yaw & 38.89 $[m/s]$ Turb. Viscosity Ratio:10 Turb. Intensity*:0.01
Tunnel-outlet	Stationary	Pressure-outlet	Gauge pressure: 0.0 $[Pa]$ Turb. Viscosity Ratio:10 Turb. Intensity:0.01
Vehicle	Stationary	Wall	No-slip
Tyre	Tangential Velocity	Wall	38.89 $[m/s]$
Rim	Tangential Velocity	Wall	38.89 $[m/s]$
Cup	Tangential Velocity	Wall	38.89 $[m/s]$
MRF-interface	Stationary	Wall	Rotation Rate: 129.19 $[rad/s]$
MRF-walls	Stationary	Wall	Rotation Rate: 129.19 $[rad/s]$

TABLE 3.3: Boundary conditions for MRF simulations.

since CFD results must be compared with them. The speed used by automotive industry when simulating a road vehicle is 140 km/h (38.89 m/s). At this velocity, we can assume constant density and incompressible flow.

∗ Turbulent intensity is defined as:

$$T.I. = \frac{u'}{U} \tag{3.1}$$

where

$$u' = \sqrt{\frac{1}{3}(u_x'^2 + u_y'^2 + u_z'^2)} \tag{3.2}$$

T.I. indicate the ratio between the standard deviation of the velocity fluctuations and the mean velocity.

Turbulent intensity can be classified as:

- **High-turbulence case:** High speed flow inside complex geometries like heat-exchangers and flow inside rotating machinery. Typical turbulent intensity is between 5% and 20%.

- **Medium-turbulence case:** Flow in not so complex devices like large pipes, ventilation flow etc. or low speed flows (low Reynolds Number). Typical turbulent intensity is between 1% and 5%.

- **Low-turbulence case:** Flow originating from a fluid that stands still, like a flow across a car. Typical turbulent intensity is very low, below 1%. Very high-quality wind-tunnels can also reach really low turbulence level.

3.3.3 Physical Model

This approach to simulate the rotation of the wheel is the easiest because does not require the physical rotation of the wheel. For this reason a steady simulation is available, allowing to obtain significant results even with short run time compared to the unsteady case.

Solver setup for MRF simulations is shown in Table 3.4.

Physical Model	*Solvers*	*Value*
$\Rightarrow$ Reynolds-Averaged Navier-Stokes $\Rightarrow$ K-Epsilon Turbulent $\Rightarrow$ Standard K-Epsilon Two-Layer $\Rightarrow$ Coupled Flow	Courant Number	250
$\Rightarrow$ Steady	*Stopping Criteria*	*Value*
$\Rightarrow$ Turbulent $\Rightarrow$ Two-Layer All y+ Wall Treatment $\Rightarrow$ Constant Density	Maximum Steps	2500

TABLE 3.4: Physical model for MRF simulations.

3.4 Sliding Mesh

The second model used to simulate the rotation of the wheel is the *Sliding Mesh*. In the following we will refer to this method as SM. This methodology requires the physical rotation of mesh and hence an unsteady simulation.

3.4.1 Model Preparation

Unlike the MRF case, in which the air within the rim was moved imposing a constant rotating velocity at the interface region, in this case the air within the rim is moved by the physical rotation of the wheel trims and its external surface (the one facing wheel trims). Next step is the creation of an interface box, enclosing the moving region, where the physical quantities are computed. Mesh parameters on the wheel and on the interface region should be chosen carefully. In fact, during the rotation, nodes on the interface mesh must coincide with the ones on the wheel mesh. In this case a polyhedral mesh has been used on these two regions. Polyhedral mesh ensures that across the interface the mesh is conformal and, hence, a good match between the two mesh nodes is achieved. In this way we can simulate the rotation of the air in the rim.

The interface box is then created using the pre-processor ANSA. The created box is a cylinder whose rotation axis is coincident with the one of the wheel. The resulting box will then contains the wheel trims, the front area of the tyre and the external surface of the rim. Particular attention is required in the creation of the cylindrical box since it must rotate with the same camber angle of the wheel.

In Figure 3.7 is shown how the cylindrical box has been created, with SM-Interface has

=SM-Interface	=SM-Interface	=SM-Interface
		=SM-Walls
(A) *Wheel front 3D view.*	(B) *Wheel back 3D view.*	(C) *Wheel section view.*
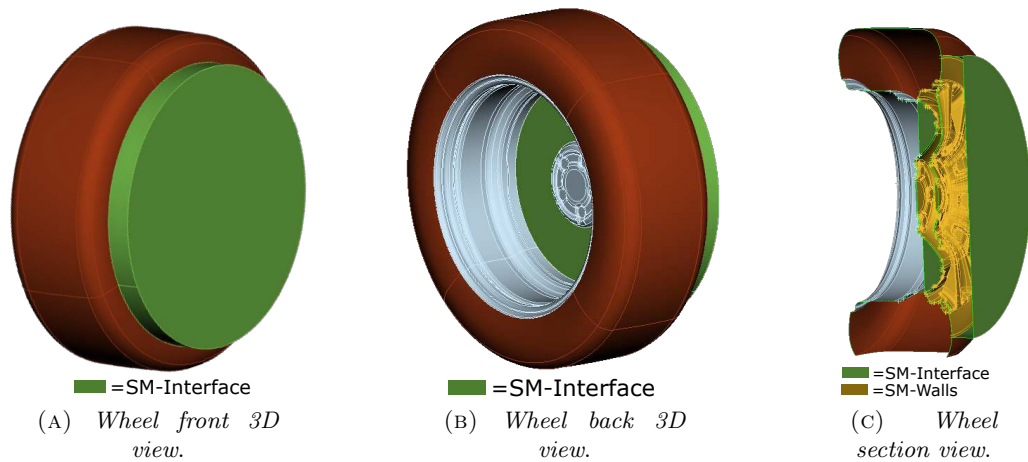
FIGURE 3.7: Wheel for SM methodology.

been indicated the box while with SM-Walls all of it contains.

3.4.2   Boundary Conditions

Boundary conditions are the same that have been showed in Table 3.3, the only difference being in MRF regions which are replaced by SM regions requiring then a change in the imposed motion. In fact in this case a rotational motion must be created in order to impose the physical rotation of the sliding mesh regions. New boundary conditions are summarized in Table 3.5.

Surface	Movement	Type	Condition
Tunnel-wall	Stationary	Wall	Slip
Tunnel-ground	Constant x-velocity	Wall	No-slip Velocity: 38.89 $[m/s]$
Tunnel-inlet	stationary	Velocity-inlet	0° yaw & 38.89 $[m/s]$ Turb. Viscosity Ratio:10 Turb. Intensity:0.01
Tunnel-outlet	stationary	Pressure-outlet	Gauge pressure: 0.0 $[Pa]$ Turb. Viscosity Ratio:10 Turb. Intensity:0.01
Vehicle	Stationary	Wall	No-slip
Tyre	Tangential Velocity	Wall	38.89 $[m/s]$
Rim	Tangential Velocity	Wall	38.89 $[m/s]$
SM-interface	Rotate	Wall	Rotation Rate: 129.19 $[rad/s]$
SM-walls	Rotate	Wall	Rotation Rate: 129.19 $[rad/s]$

TABLE 3.5: Boundary conditions for SM simulations.

3.4.3   Physical Model

In this type of methodology a different approach is required since we are solving an unsteady simulation. In such simulation a given physical rotation time is simulated. This requires to define a time-step that indicates how often the simulated object is displaced. For each time-step some inner iterations are performed since we are executing an implicit numerical method.

To ensure greater solution convergence, a steady approach has been used for the first 1000 iterations and successively the unsteady simulation has been performed.

Table 3.6 shows solver setup used in SM simulations.

Physical Model	Solvers	Value
⇒ Detached Eddy Simulation		Time Step: $2.0e^{-4}$ s
⇒ All $y+$ Wall Treatment	Implicit Unsteady	
⇒ Exact Wall Distance		Discretization: 2nd-order
⇒ Segregated Flow	*Stopping Criteria*	*Value*
⇒ Turbulent	Maximum Inner Iteration	7
⇒ Implicit Unsteady		
⇒ Constant Density	Maximum Physical Time	2.5

TABLE 3.6: Physical model for SM simulations.

3.5 Overset

Third and last methodology used to simulate the rotation of the wheel is the Overset. This model, in contrast with the other two, allows the physical rotation of the wheel and, hence, a better representation of the real model. As in the sliding mesh model this requires an unsteady simulation but more run time.

In the following we will use OS when referring to the overset model.

3.5.1 Model Preparation

In section 2.5.3 it has been explained that, for this model, a background and an overset box are necessary . The background box, i.e. the domain where the solution is computed, is the wind tunnel, which contains the car without the wheels.

Overset box is then created using the pre-processor ANSA. The Overset box, shown in Figure 2.2, will contain the entire wheel: rim, tyre and wheel trims.

In the creation of the box particular attention has been put in the area near the break disc since this could intersect the box. For this reason a morphing operation has been performed in order to reduce disc and calliper brake. In Figure 3.8(B) is shown a section representation of the wheel and we can see that the disc break is very close to the box wall. An other aspect to consider is the camber of the wheel that must be maintained during the overset box creation.

In Figure 3.8 we can see that, differently from previous two cases, the tyre now intersect the ground without applying a truncation. In this case in fact, at every time-step of the simulation, there is a coupling between the tyre and the ground given by the imposition of a Zero Gap interface between the overset and the background region.

(A) *Whee 3D view.*

(B) *Wheel section view.*
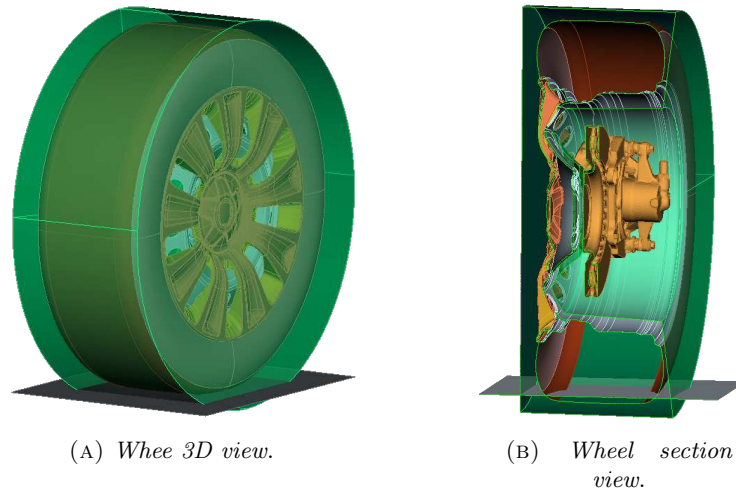
FIGURE 3.8: Overset Box.

Polyhedral Cell Mesher						
Parameters	*Standard Value*	*Ground around the wheel*	*Ground*	*External Style*	*Interface*	*Wind Tunnel*
Base Size	X [m]					
Target Surface size *	15%	7.5%	20/45/ 250/500%	10%	5%	1000%
Minimum Surface size *	5%	7.5%	20/45/ 250/500%	5%	2%	1000%
Number of Prism Layer	4	8	11	11	Disable	Disable
Prism Layer Near Wall Thickness *	0.3%	0.2%	0.3%	0.3%		
Prism Layer Near Total Thickness *	3%	5%	10%	10%		

* Values relative to base

TABLE 3.7: Polyhedral cell mesher parameters for vehicle.

Polyhedral Cell Mesher				
Parameters	*Standard Value*	*Box Overset*	*Tyre*	*Cup Rim*
Base Size	X [m]			
Target Surface size *	15%	4%	2%	2%
Minimum Surface size *	5%	2%	2%	2%
Number of Prism Layer	10	PV[#]	PV	PV
Prism Layer Near Wall Thickness *	0.2%			
Prism Layer Near Total Thickness *	5%			

* Values relative to base
#PV=Parent Values

TABLE 3.8: Polyhedral cell mesher parameters for wheel.

3.5.2 Mesh Preparation

In this model, a critical factor is the meshes generation since is necessary to have enough cells across the overlapping zone between background and overset region. A good number of cell layers in both background and overset mesh is at least $4 - 5$. In order to minimize

the discretization error is preferable that the cell size on both meshes are similar within the overlapping zone. During the mesh generation the main problem that may occur is: if the mesh is coarse, we could find some acceptor cells out of the boundary between background and overset region while if the mesh is too fine we could have inactive donor cells.

To ensure greater interpolation between the two regions is necessary that background and overset regions meshes are generated with different mesh continuum since during the ZeroGap interface initialization these are overlapped before the final mesh is created. During the mesh generation it was noted that, due to the rotation of the wheel, the area of intersection between the tyre and the ground was the most problematic one and, hence, a particular attention was required for the setting of mesh parameters. In this case a better interpolation was ensured with a polyhedral mesh whose main parameters, for vehicle and wheel, are shown in Tables 3.7 and 3.8.

3.5.3 Boundary Conditions

Surface	Movement	Type	Condition
Tunnel-wall	Stationary	Wall	Slip
Tunnel-ground	Constant x-velocity	Wall	No-slip Velocity: 38.89 $[m/s]$
Tunnel-inlet	stationary	Velocity-inlet	0° yaw & 38.89 $[m/s]$ Turb. Viscosity Ratio:10 Turb. Intensity:0.01
Tunnel-outlet	stationary	Pressure-outlet	Gauge pressure: 0.0 $[Pa]$ Turb. Viscosity Ratio:10 Turb. Intensity:0.01
Vehicle	Stationary	Wall	No-slip
Overset-FL	Rotate	Overset Mesh	Rotation Rate: 129.19 $[rad/s]$
Overset-RL	Rotate	Overset Mesh	Rotation Rate: 129.19 $[rad/s]$
Overset-FR	Rotate	Overset Mesh	Rotation Rate: 129.19 $[rad/s]$
Overset-RR	Rotate	Overset Mesh	Rotation Rate: 129.19 $[rad/s]$

TABLE 3.9: Boundary conditions for OS simulations.

The next step, after mesh preparation, is to set boundary conditions. Unlike the steady simulation, in this case a physical rotation of the overset box is required. For every wheel, a rotational motion, in its own local reference frame, was created. Another condition that has been imposed at the overset region is the type, i.e. 'Overset Mesh'.

Last step in the setting the overset model is the creation of the ZeroGap interfaces. Table 3.9 shows the new boundary conditions for a short representation.

3.5.4   Physical Model

For Overset model such as the sliding mesh case an unsteady simulation is required. In Table 3.10 are shown solver setting used. In this case to improve the convergence of the solution different time step have been used during the simulation. In an initial equilibration part (i.e. $t < 0.001s$) a time step of $0.000025s$ was used. Afterwards the time step is increased to a value of $0.00025s$.

Physical Model	*Solvers*	*Value*
$\Rightarrow$ Detached Eddy Simulation		Time Step: $if\ t < 0.001s \Rightarrow$
$\Rightarrow$ All $y+$ Wall Treatment	Implicit Unsteady	$\Rightarrow 0.000025s\ else\ 0.00025s$
$\Rightarrow$ Exact Wall Distance		Discretization: 2nd-order
$\Rightarrow$ Segregated Flow	*Stopping Criteria*	*Value*
$\Rightarrow$ Turbulent	Maximum Inner Iteration	8
$\Rightarrow$ Implicit Unsteady		
$\Rightarrow$ Constant Density	Maximum Physical Time	$\approx 1.9\ s$

TABLE 3.10: Physical model for OS simulations.

3.5.5   Overset Cell Type

Once the mesh is generated, before running the simulation, a check of mesh parameters is performed. CFD code provides a function, called Overset Cell Type, that allows to inspect the mesh and to identify the status of the cells. In particular this function provides a numerical scale, from -3 to 3, with the following meaning:

- 0 active cell;

- -1 inactive cell that resides outside of the background mesh;

- -2 inactive cell that is covered by another overset region. Consequently, this type can only occur for multiple overset meshes;

- -3 inactive cell inside a zero gap zone;

- 1 donor cell;

- 2 active, intermediate cell layer used by the hole cutting[1] process.

- 3 acceptor cell.
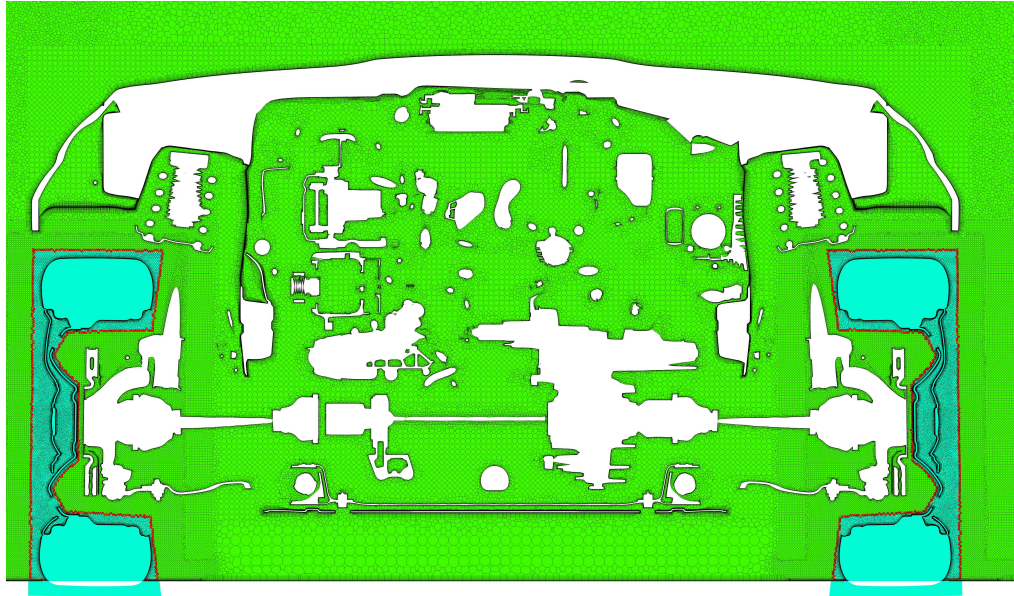
(A) *Overset Cell Type front wheel section.*
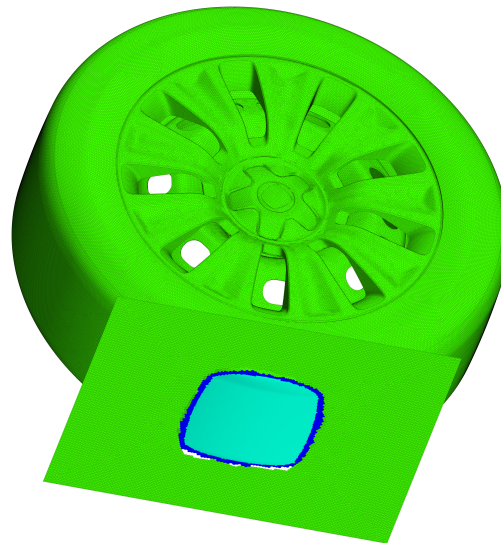
(B) *Overset Cell Type in Zero Gap area.*
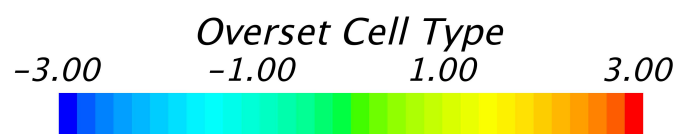
FIGURE 3.9: Overset Cell Type.

---

[1]The hole cutting is the process that allows to determine whether cells are active or inactive in the coupled simulation.

In Figure 3.9(A) we can see, as an example, a section plane of the front car by which we can evaluate the meshes accuracy. In the same figure we can notice that acceptor cells, i.e. the red cells, are arranged around the boundary of the overset box and they are not present in any other place. In fact the presence of acceptor cell in the background region would means that the mesh is too coarse. Green cells are the active ones and they are the cells in which the solution is computed. Cyan cells are the inactive ones and became active when the overset box is moved.

In Figure 3.9 (B), where the Zero Gap area is shown, we can see that at the contact between the tyre and the ground cells are blue. This indicate the inactive cells in the Zero Gap region which are arranged around the boundary of the contact zone.

Chapter 4

Results

In this chapter, after a brief overview of the generic results about the coefficients distribution, we will show the main results obtained with the different methodologies used for the rotation of the wheel.

Results will be compared to wind tunnel tests with the aid of CFD visualizations and numerical calculations. In particular the ΔC_D between different configurations, see Table 3.1, are compared.

4.1   Baseline Coefficients Distribution

First of all in Figure 4.1 we can see a generic pressure coefficient distribution around the car. This representation has been obtained with the MRF methodology. From the figure we can notice that the parts providing the greatest contribution to the drag are: front bumper, side mirrors, frontal area of the wheels and windscreen. In fact, this zones are the ones where the flow impacts perpendicular to the surfaces and, hence, where a stagnation point occurs.

In Figure 4.1(B) we can also see the effect of the front middle dam, namely the creation of a depression zone behind it.

In Figure 4.2 are shown the distributions of the drag coefficients for the complete vehicle, external body, under body and under hood. This coefficients are normalized by the average C_D, computed with MRF model, of the NP configuration. From the figure we can see that the maximum amount of accumulated C_D is in the front of the car.
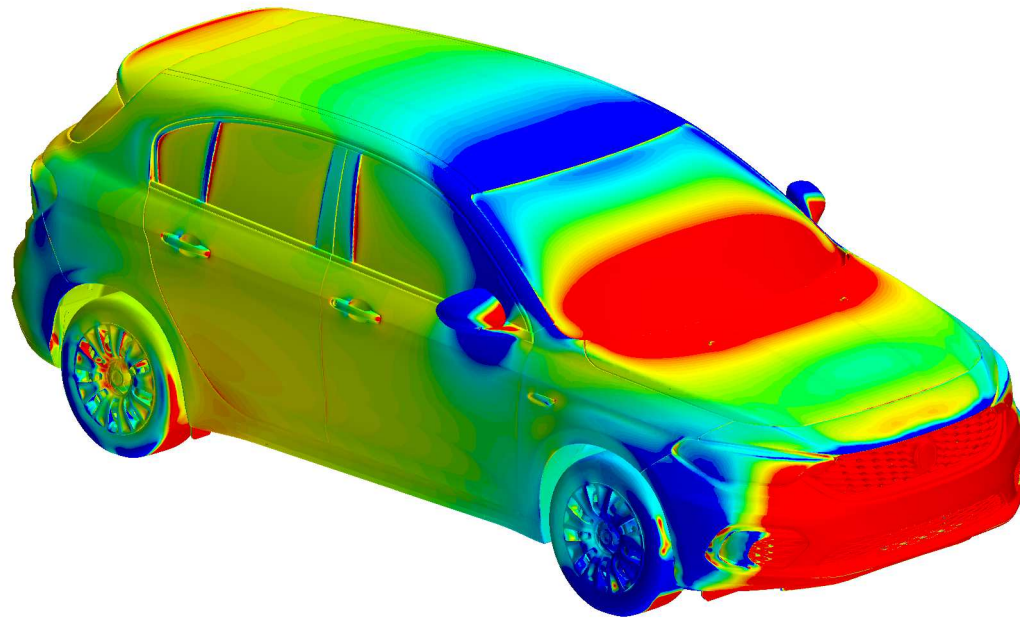
(A) *External Body.*

(B) *Under Body.*

Pressure Coefficient

| −0.500 | −0.400 | −0.300 | −0.200 | −0.100 | 0.00 |
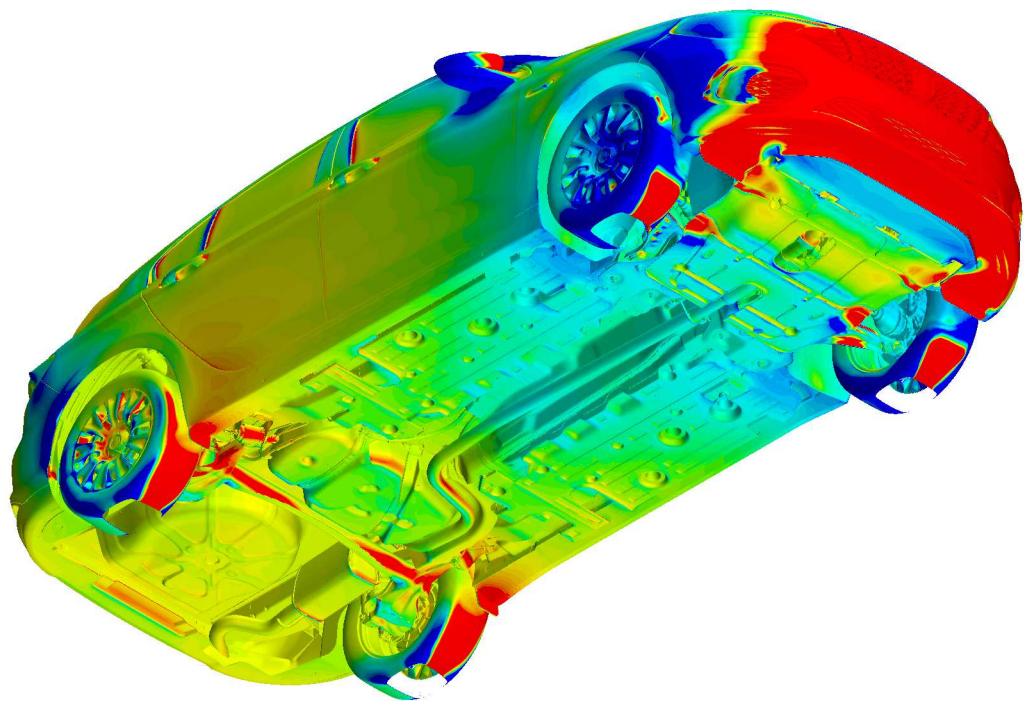
FIGURE 4.1: Pressure Coefficient distribution.
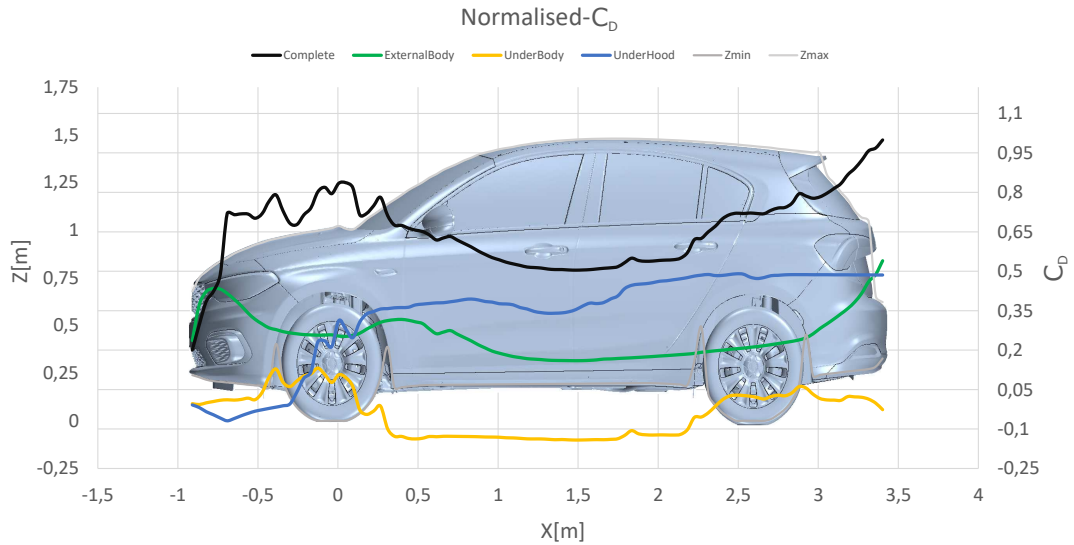
FIGURE 4.2: Normalised C_D accumulated along the longitudinal axis.

Contributions to the total accumulated C_D are: $\approx 54\%$ from the external body, $\approx 48\%$ from the under hood and $\approx -2\%$ from the under body.

4.2 Moving Reference Frame

In this section are shown the results obtained, for the different configurations, adopting the MRF model.

In Figure 4.3 is reported the convergence of the coefficient drag for the NP configurations. Since the MRF simulations are steady, we can note that the coefficient drag begin to reach convergence after 1000 iterations.

For this methodology the total C_D, normalized with the experimental coefficient, is:

$$C_D = 0.982$$

Numerical and experimental values of ΔC_D are reported in Table 4.1.

To understand the behaviour of the flow around the wheels and how the MRF methodology approximate the flow features, we can visualize the distribution of the principal physical quantities. These visualizations are compared with the ones obtained during experimental tests. Pressure coefficient and velocity scenes for the NP configuration are shown in Figures 4.4, 4.5, 4.6, 4.7, 4.8, 4.9, 4.10, 4.11 and 4.12. From the visualizations we can see a substantial difference between the MRF model and experiments, however

Case		$\Delta C_{D_{MRF}}\%$	$\Delta C_{D_{WT}}\%$	$Err\ \%$
002	NP+Air Curtains Closed	0.85	−0.63	1.49
003	NP+No Front Wheel Spats	4.56	2.85	1.71
004	NP+No Front Air Dam	−0.76	−0.95	0.19
005	NP+No Engine Shield	1.17	1.90	0.73
006	NP+No Wheel Trims	3.29	1.27	2.03

<div align="center">

Run Time $\approx 6h$

Processor No. 252

</div>

TABLE 4.1: MRF results normalised by experimental total C_D.

if we look at the numerical results in Table 4.1 we can note that the percentage error, except for one case, is less than 2%.
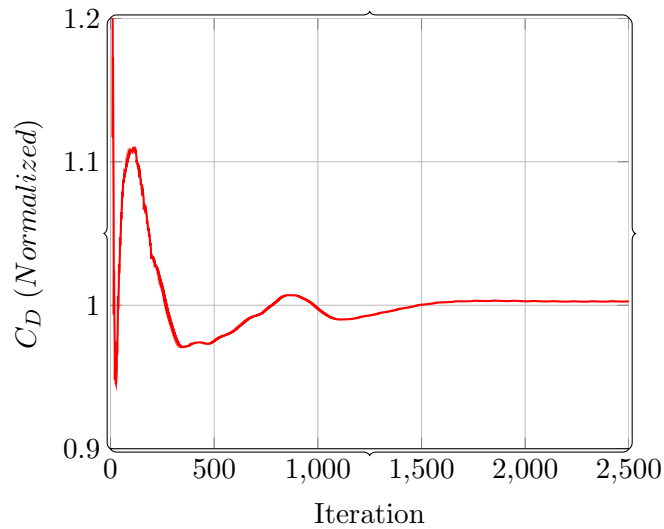
FIGURE 4.3: Coefficient Drag for MRF case and NP configuration.

(A) *Experimental.*   (B) *MRF methodology.*
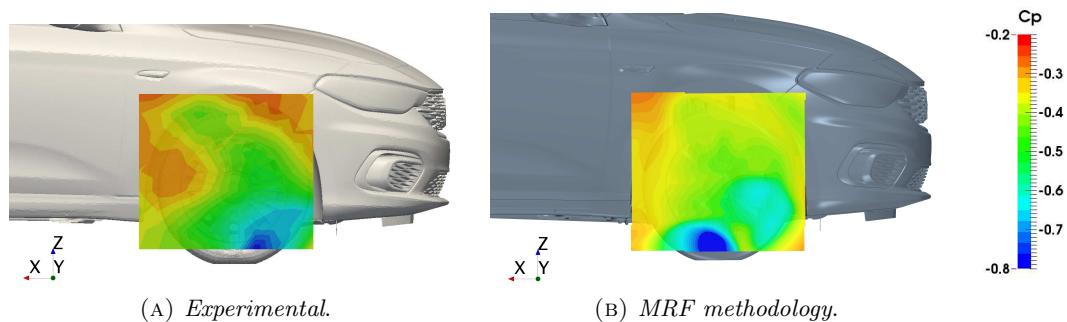
FIGURE 4.4: MRF-Front right wheel pressure coefficient distribution in the xz plane at $y = 0.93\ m$.

(A) *Experimental.*   (B) *MRF methodology.*
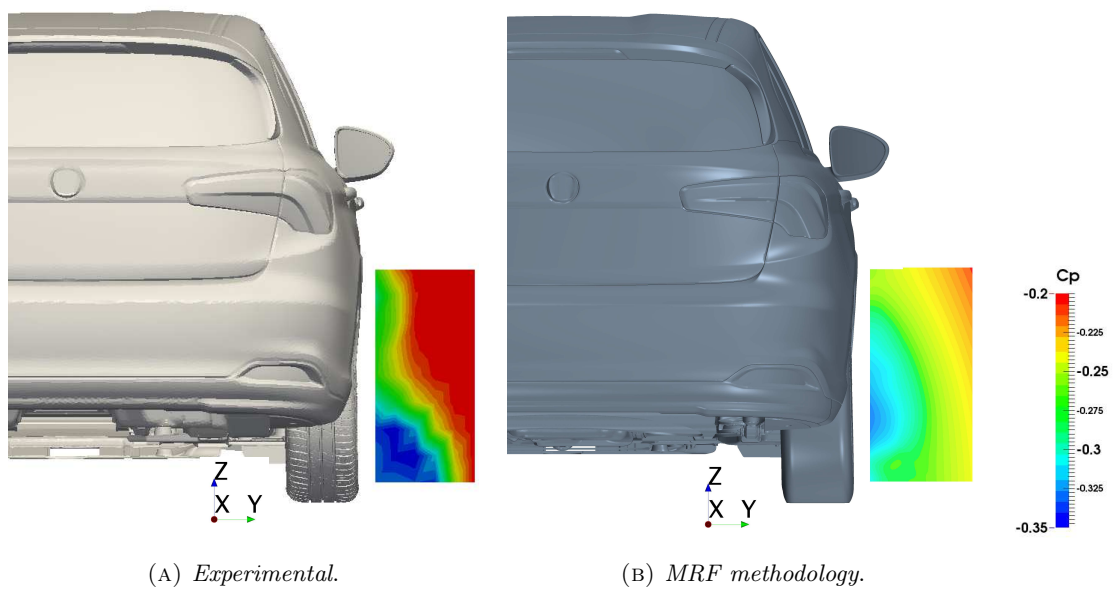
FIGURE 4.5: MRF-Front right wheel pressure coefficient distribution in the yz plane at $x = 0.42\ m$.

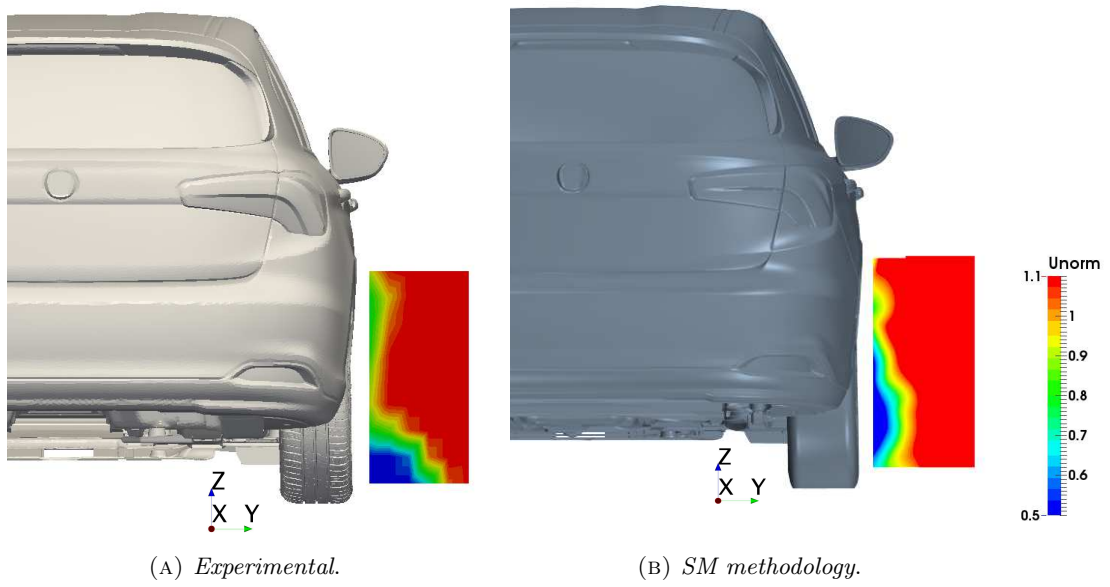(A) *Experimental.*   (B) *MRF methodology.*
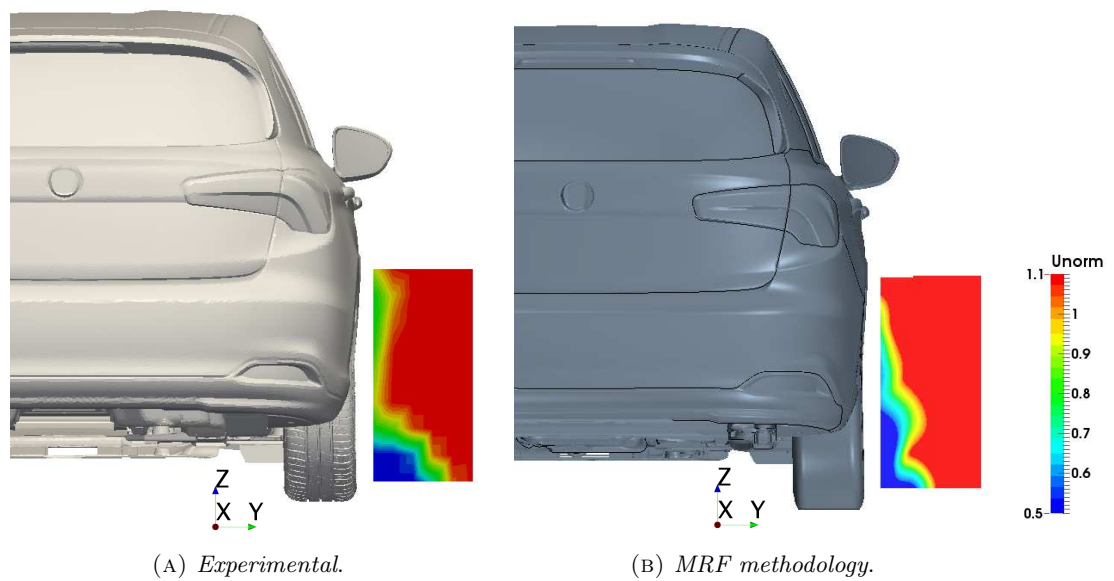
FIGURE 4.6: MRF-Front right wheel normalized velocity-x distribution in the yz plane at $x = 0.42\ m$.

(A) *Experimental.*

(B) *MRF methodology.*

FIGURE 4.7: MRF-Front right wheel pressure coefficient distribution in the xy plane at $z = 0.05\ m$.

(A) *Experimental.*

(B) *MRF methodology.*

FIGURE 4.8: MRF-Front right wheel normalized velocity distribution in the xy plane at $z = 0.05\ m$.
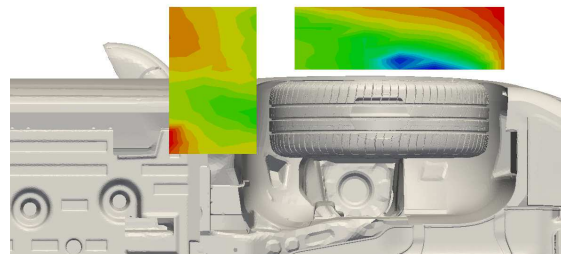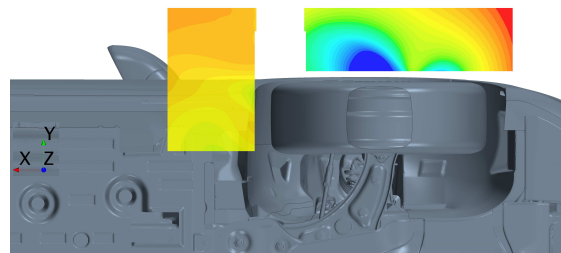
(A) *Experimental.*
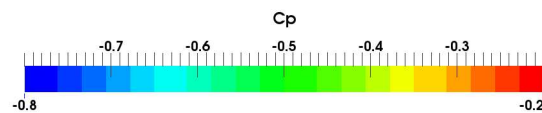
(B) *MRF methodology.*

FIGURE 4.9: MRF-Front right wheel pressure coefficient distribution in the xy plane at $z = -0.21\ m$.
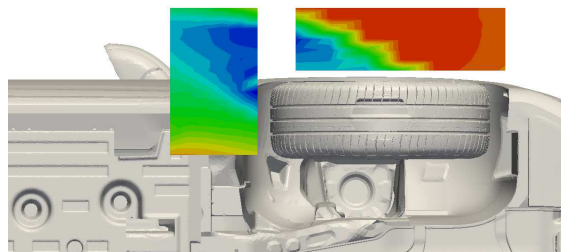
(A) *Experimental.*
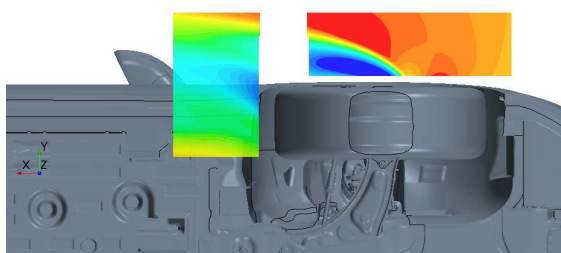
(B) *MRF methodology.*
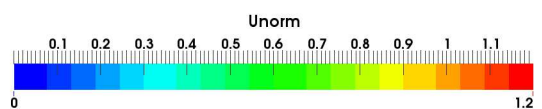
FIGURE 4.10: MRF-Front right wheel normalized velocity-x distribution in the xy plane at $z = -0.21\ m$.

(A) *Experimental.*   (B) *MRF methodology.*
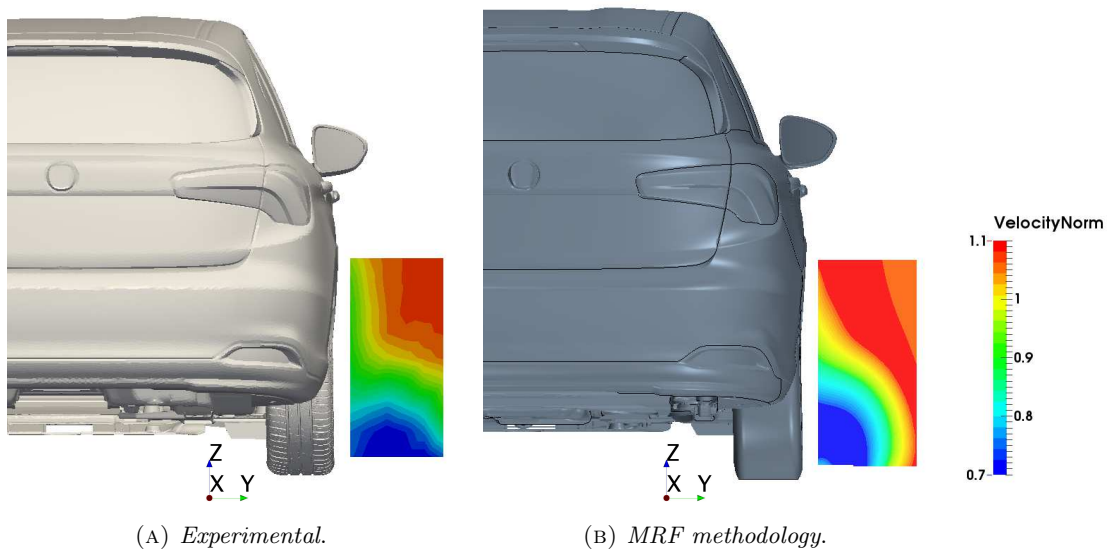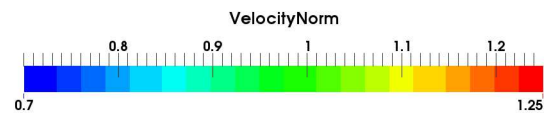
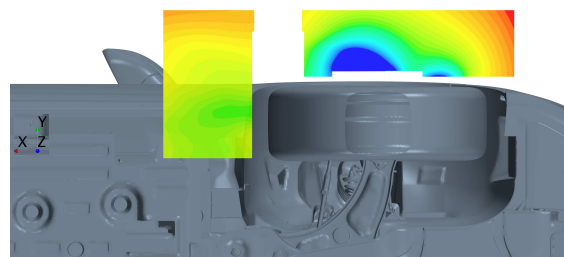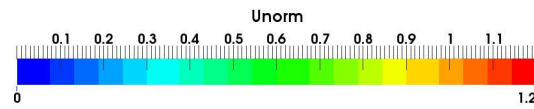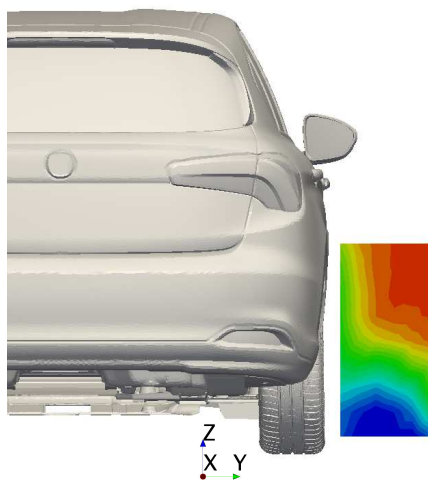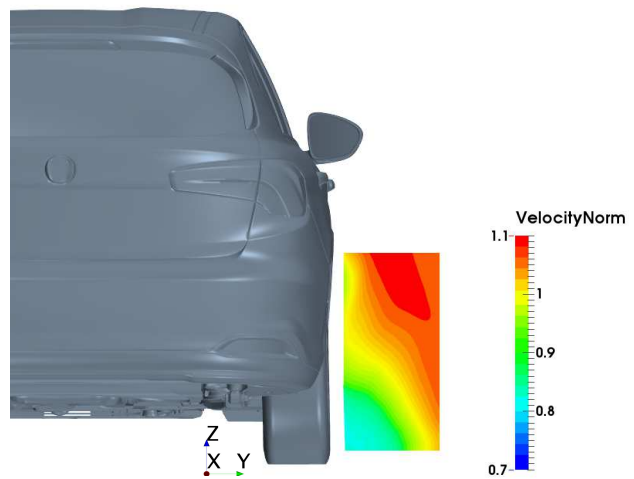FIGURE 4.11: MRF-Rear right wheel normalized velocity distribution in the yz plane at $x = 2.56\ m$.

(A) *Experimental.*   (B) *MRF methodology.*
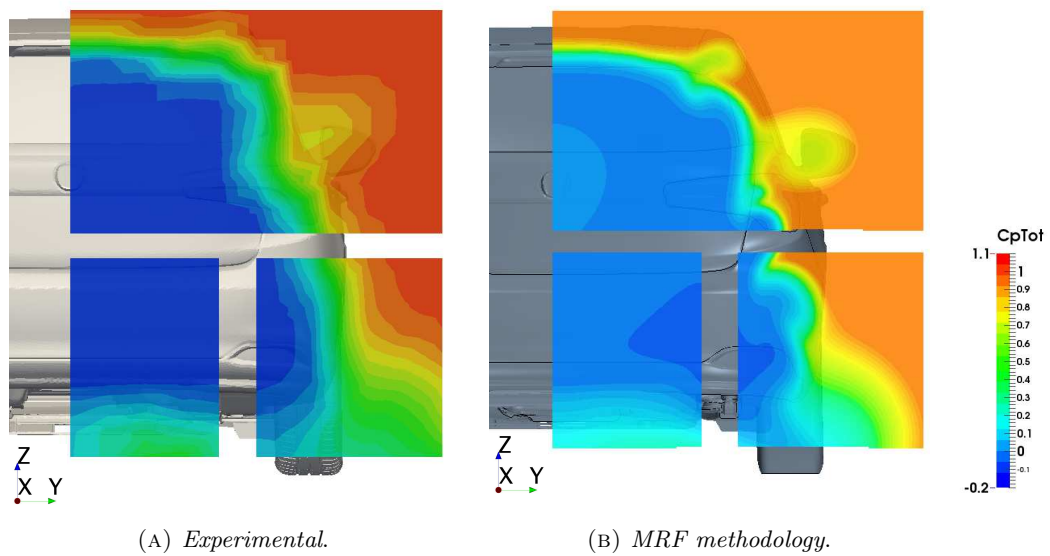
FIGURE 4.12: MRF-Rear car total pressure coefficient distribution in the yz plane at $x = 3.53\ m$.

4.3   Sliding Mesh

In this section, as the previous, are presented the results obtained with the sliding mesh model.

To compute the coefficient drag for the sliding mesh case, because of the unsteady simulation, is necessary to determinate the average of the coefficients computed at each time step of the simulation. In Figure 4.13 we can see, for the NP configuration, how the normalized coefficient drag oscillates around the average value after $1\ s$.

In this case the total C_D, normalized with the experimental coefficient, is:

$$C_D = 1.098$$
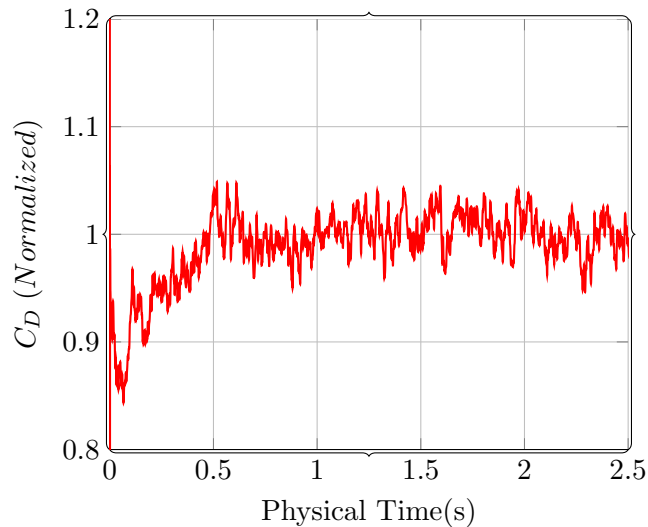
FIGURE 4.13: Coefficient Drag for sliding mesh case and NP configuration.

Results are shown in Table 4.2. By looking at the percentage error, which is now about 1 %, we can detect an improvement compared to the MRF results.

Representation of the principal physical quantities, which are now visualized as average values computed over all the simulated time, are shown in Figures 4.14, 4.15, 4.16, 4.17, 4.18, 4.19, 4.20, 4.21 and 4.22. From the visualization we can note that the SM, compared to MRF, provides a better representation of the flow features since the unsteady simulation, respect to steady one, better captures the turbulent flow.

Case		$\Delta C_{D_{SM}}\%$	$\Delta C_{D_{WT}}\%$	*Err* %
002	NP+Air Curtains Closed	0.31	−0.63	0.94
003	NP+No Front Wheel Spats	2.06	2.85	0.79
004	NP+No Front Air Dam	−0.08	−0.95	0.87
005	NP+No Engine Shield	0.47	1.90	1.43
006	NP+No Wheel Trims	0.42	1.27	0.85

Run Time $\approx 110h$

Processor No. 252

TABLE 4.2: Sliding Mesh results normalised by experimental total C_D.

(A) *Experimental.*

(B) *SM methodology.*
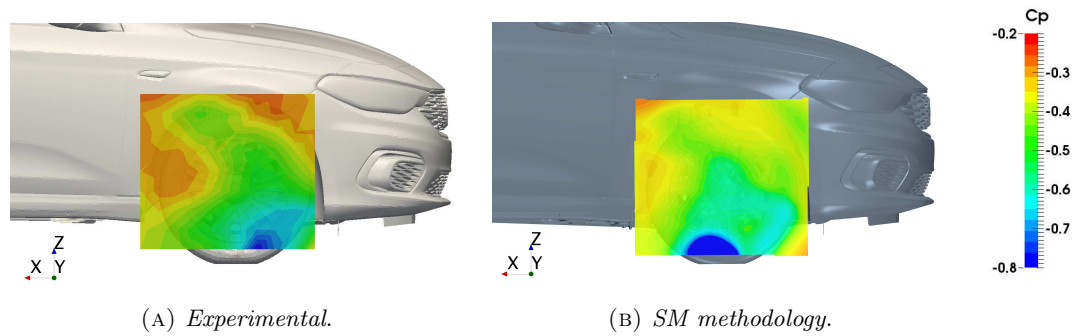
FIGURE 4.14: SM-Front right wheel pressure coefficient distribution in the xz plane at $y = 0.93\ m$.

(A) *Experimental.*

(B) *SM methodology.*
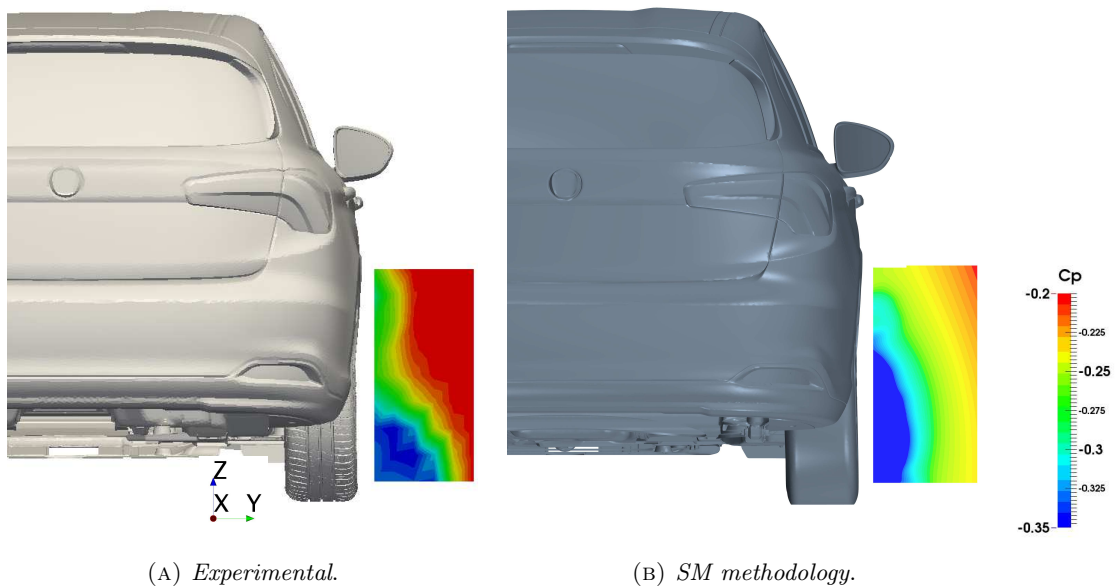
FIGURE 4.15: SM-Front right wheel pressure coefficient distribution in the yz plane at $x = 0.42\ m$.

(A) *Experimental.*   (B) *SM methodology.*

FIGURE 4.16: SM-Front right wheel normalized velocity-x distribution in the yz plane at $x = 0.42\ m$.

(A) *Experimental.*
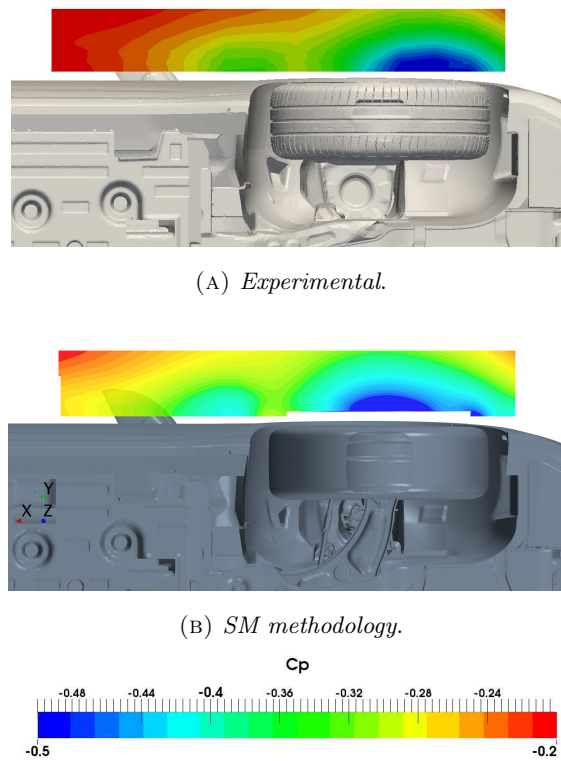
(B) *SM methodology.*

FIGURE 4.17: SM-Front right wheel pressure coefficient distribution in the xy plane at $z = 0.05\ m$.
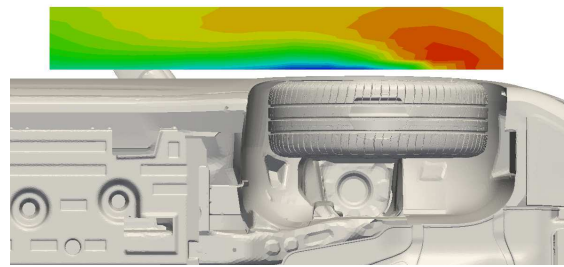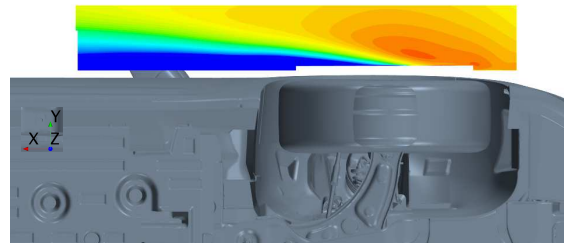
(A) *Experimental.*

(B) *SM methodology.*

FIGURE 4.18: SM-Front right wheel normalized velocity distribution in the xy plane at $z = 0.05\ m$.
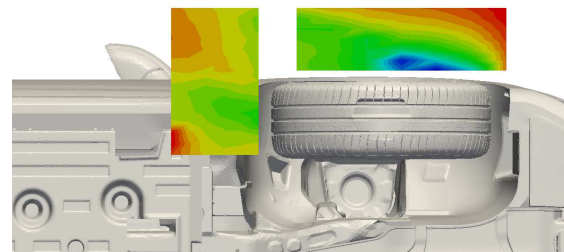
(A) *Experimental.*
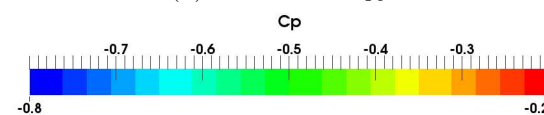
(B) *SM methodology.*

FIGURE 4.19: SM-Front right wheel pressure coefficient distribution in the xy plane at $z = -0.21\ m$.
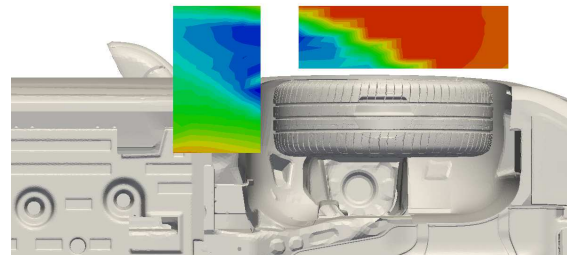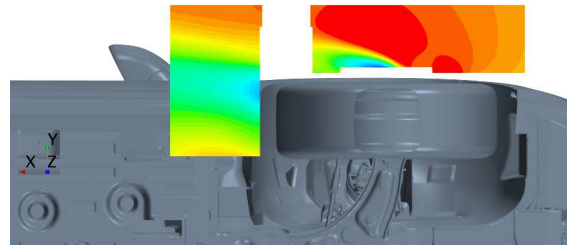
(A) *Experimental.*

(B) *SM methodology.*

FIGURE 4.20: SM-Front right wheel normalized velocity-x distribution in the xy plane at $z = -0.21\ m$.

(A) *Experimental.*   (B) *SM methodology.*

FIGURE 4.21: SM-Rear right wheel normalized velocity distribution in the yz plane at $x = 2.56\ m$.

(A) *Experimental.* (B) *SM methodology.*
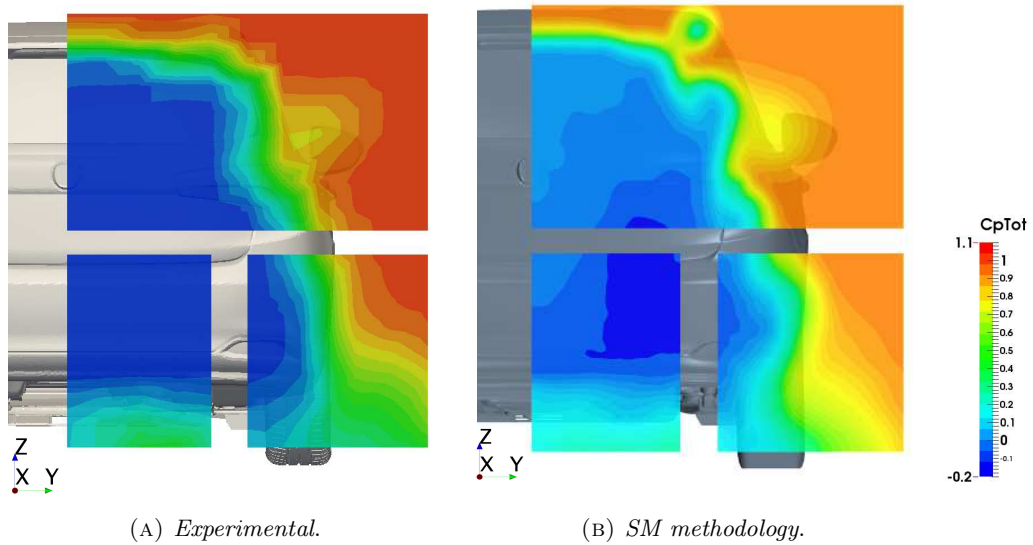
FIGURE 4.22: SM-Rear car total pressure coefficient distribution in the yz plane at $x = 3.53\ m$.

4.4 Overset

In this section are presented the results obtained with the overset model.

To compute the coefficient drag in the overset case, because of the unsteady simulation, is necessary to determinate the average of the coefficients computed at every time step of the simulation. In Figure 4.23 we can see, for the NP configuration, how the normalized coefficient drag oscillates around the average value after $0.8\ s$.

In this case the total C_D, normalized with the experimental coefficient, is:

$$C_D = 1.082$$

For this model, because of the longest run time compared to the sliding mesh, only the coefficient drag of one aerodynamic enabler has been computed. Results are shown in Table 4.3. As it can be seen, the percentage error is increased compared to sliding mesh and MRF models.

Representation of the principal physical quantities, which are now visualized as average values computed over all the simulated time, are shown in Figures 4.24, 4.25, 4.26, 4.27, 4.28, 4.29, 4.30, 4.31 and 4.32. From these visualizations we can see that the OS capture more accurately than SM and MRF cases the turbulent flow. It must be noticed that,

even tough OS provides a much more accurate flow features, the same accuracy is not found in numerical results for the drag coefficient. Considering that the necessary run time for OS simulations is much greater compared to other methods such method doesn't represent the optimal choice.
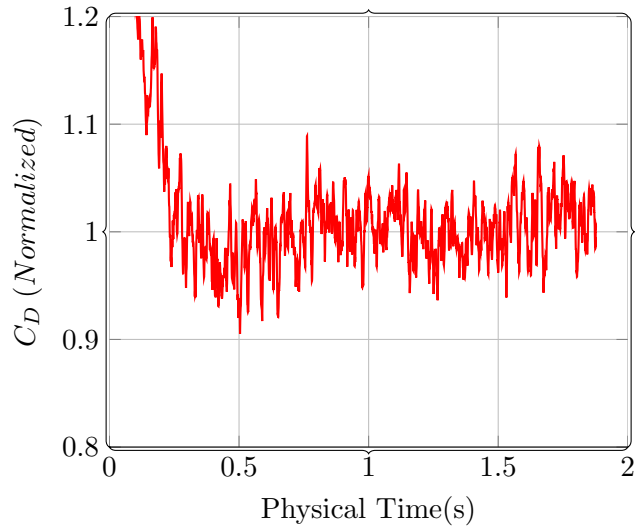
FIGURE 4.23: Coefficient Drag for overset case and NP configuration.

	Case	$\Delta C_{D_{OS}}\%$	$\Delta C_{D_{WT}}\%$	Err %
005	NP+No Engine Shield	−0.56	1.90	2.46
	Run Time $\approx 498h$			
	Processor No. 756			

TABLE 4.3: Overset results normalised by experimental total C_D.

(A) *Experimental.*   (B) *OS methodology.*
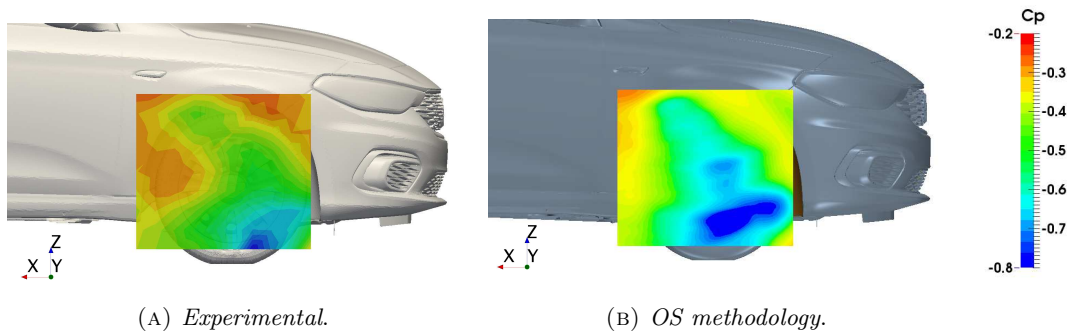
FIGURE 4.24: OS-Front right wheel pressure coefficient distribution in the xz plane at $y = 0.93\ m$.

(A) *Experimental.*   (B) *OS methodology.*
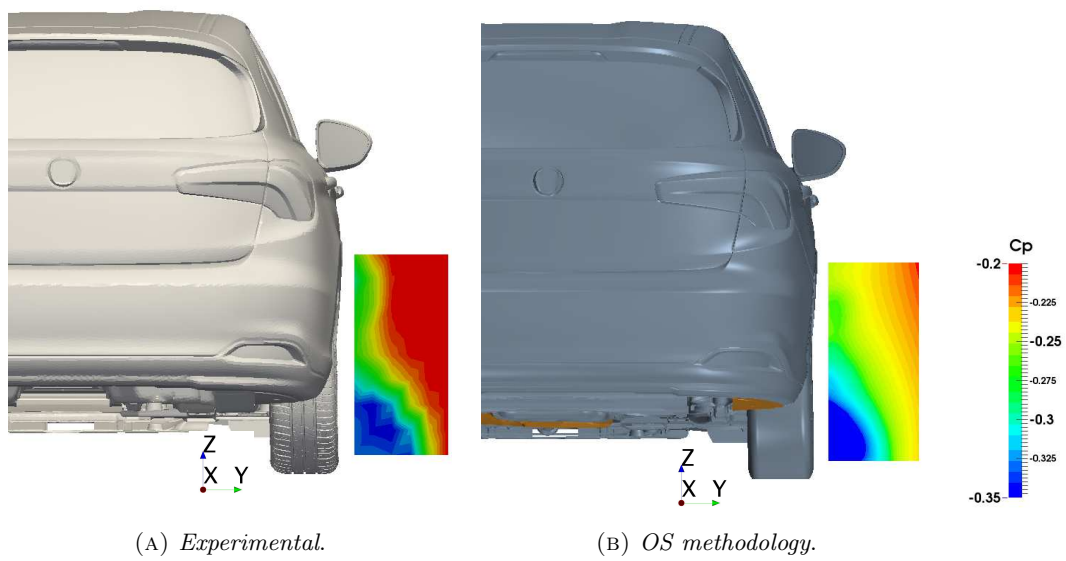
FIGURE 4.25: OS-Front right wheel pressure coefficient distribution in the yz plane at $x = 0.42\ m$.
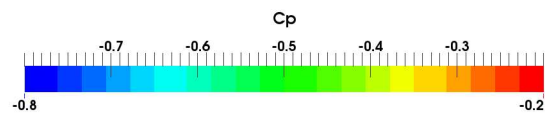

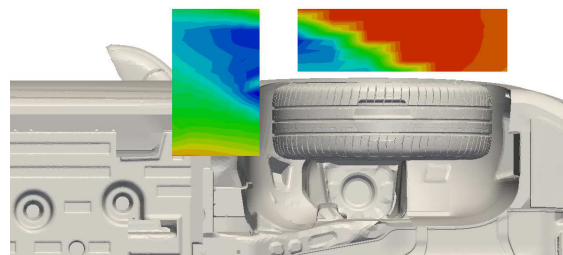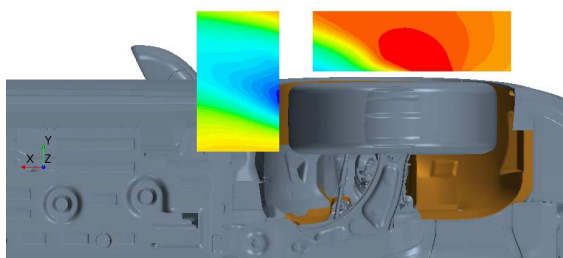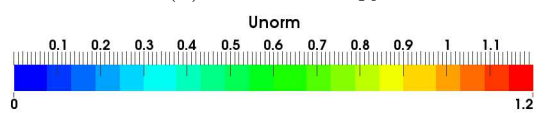(A) *Experimental.*   (B) *OS methodology.*
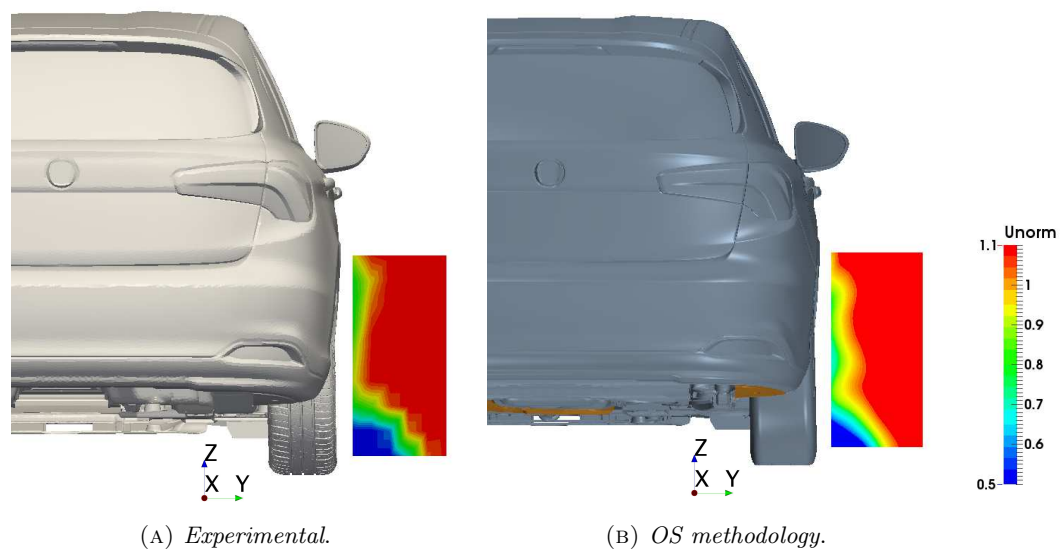
FIGURE 4.26: OS-Front right wheel normalized velocity-x distribution in the yz plane at $x = 0.42\ m$.
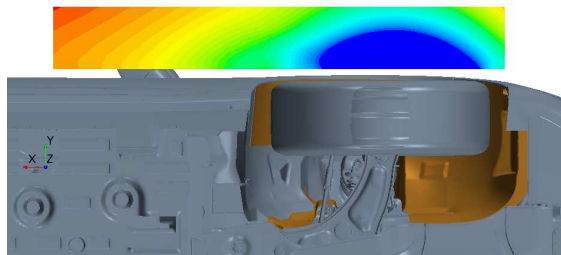
(A) *Experimental.*
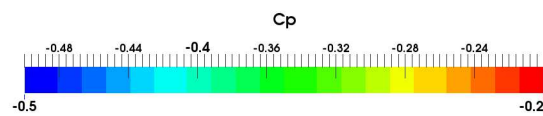
(B) *OS methodology.*

FIGURE 4.27: OS-Front right wheel pressure coefficient distribution in the xy plane at $z = 0.05\ m$.
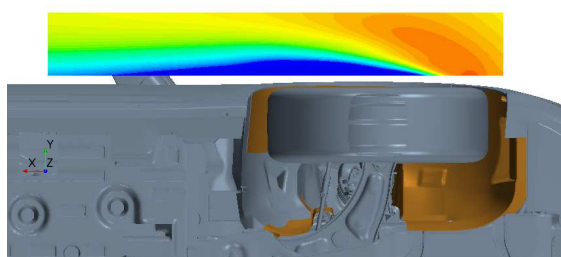
(A) *Experimental.*
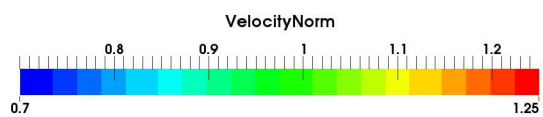
(B) *OS methodology.*

FIGURE 4.28: OS-Front right wheel normalized velocity distribution in the xy plane at $z = 0.05\ m$.
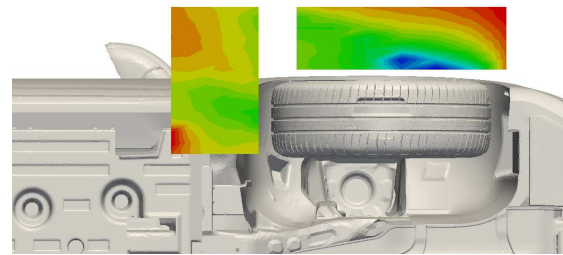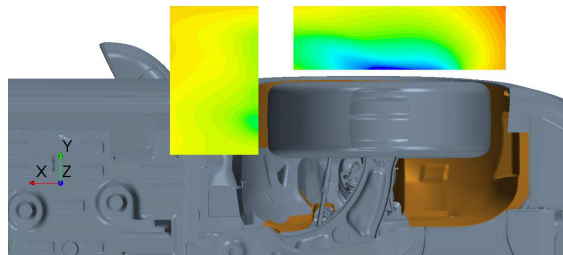
(A) *Experimental.*

(B) *OS methodology.*

FIGURE 4.29: OS-Front right wheel pressure coefficient distribution in the xy plane at $z = -0.21\ m$.

(A) *Experimental.*

(B) *OS methodology.*

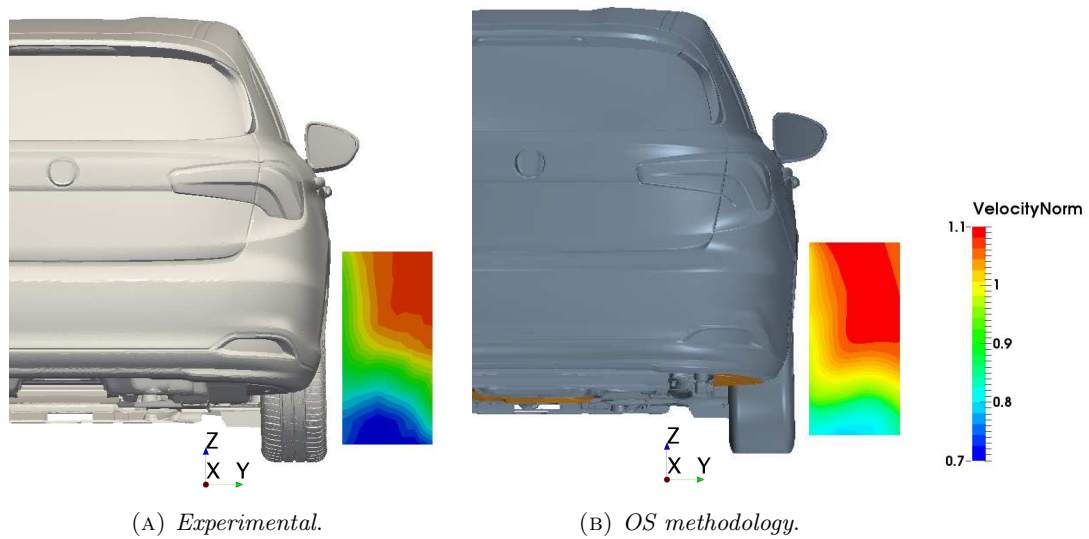FIGURE 4.30: OS-Front right wheel normalized velocity-x distribution in the xy plane at $z = -0.21\ m$.

(A) *Experimental.*   (B) *OS methodology.*

FIGURE 4.31: OS-Rear right wheel normalized velocity distribution in the yz plane at $x = 2.56\ m$.

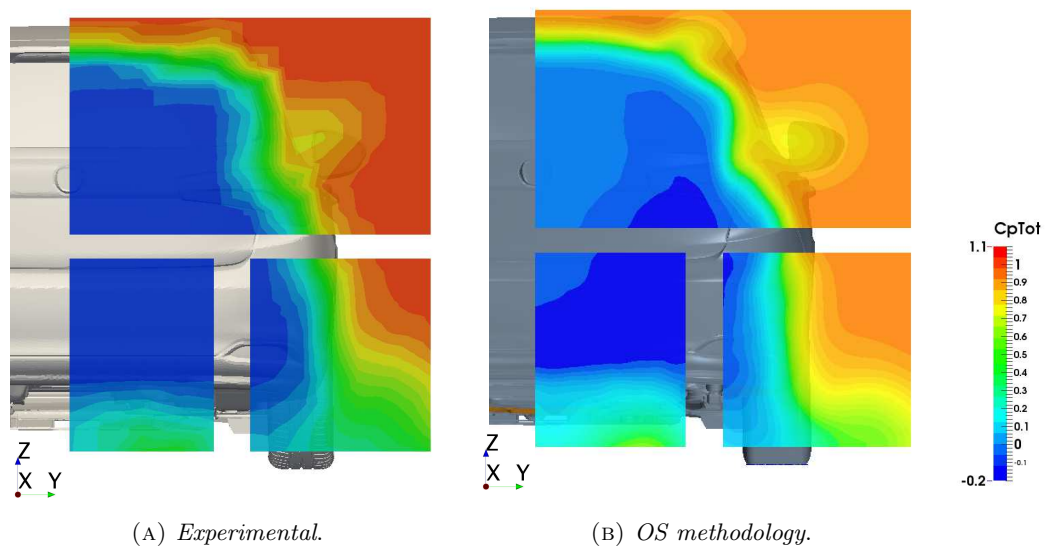(A) *Experimental.*   (B) *OS methodology.*

FIGURE 4.32: OS-Rear car total pressure coefficient distribution in the yz plane at $x = 3.53\ m$.

4.5 Further Configurations

In order to validate the CFD results with the experimental ones, other two different configurations of engine shield, in addition to the NP configuration, have been adopted. In particular the difference between the three configurations is in the section profile.

The three shields compared are shown in 4.33.

For this cases only the MRF and sliding mesh methodology has been tested since the overset model would required much more run time.
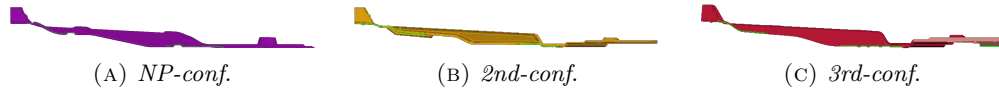
Obtained results are summarized in Table 4.4.

(A) *NP-conf.*   (B) *2nd-conf.*   (C) *3rd-conf.*

FIGURE 4.33: Engine shields section view.

Case	$\Delta C_D\%$			$\Delta C_{D_{WT}}\%$	$Err\%$		
	MRF	*SM*	*OS*		*MRF*	*SM*	*OS*
NP-conf	−1.17	−0.47	0.56	−1.90	0.73	1.43	2.46
2nd-conf	−1.39	0.16		1.58	2.97	1.42	
3rd-conf	−1.39	−2.58		−1.27	0.13	1.32	

TABLE 4.4: Engine shields results normalised by experimental total C_D.

From the histogram in Figure 4.34 we can see that MRF methodology is more accurate than the sliding mesh for the third and NP configuration while for the second configuration the sliding mesh is better.[1]

To understand why the three engine shields configurations lead to an improving or a worsening of the coefficient drag, we can observe the velocity scenes in x direction, obtained with the sliding mesh case, in Figure 4.35. From the figure we can note that *NP-conf.* is the best solution compared to the other two since the shield is able to separate the flow and, hence, allows to the underbody to work in the wake which is the optimal solution for a no flat undertray. In fact, for a passenger car in which a flat undertray is not provided, an anticipate flow separation ensure that this does not separate in other zones of the underbody which would lead to a larger increase of coefficient drag. In Figure 4.36, in which a skin friction scene of underbody is displayed, we can see the effect of different way of flow separation. As expected, in the 2nd and 3rd configurations there are more zones than in the NP configuration where the skin friction presents higher values .

---

[1]The wind tunnel results for 2nd and 3rd configurations have been obtained with a different car configuration compared to numerical one.
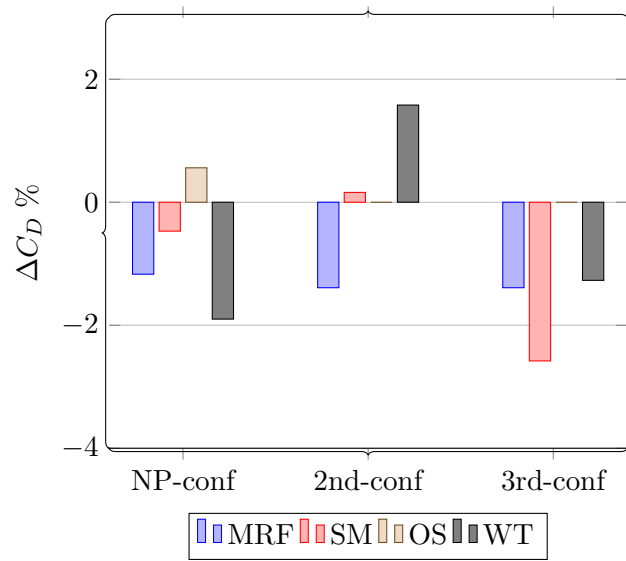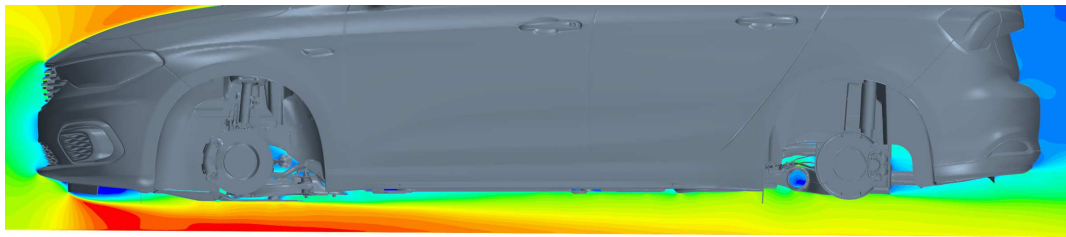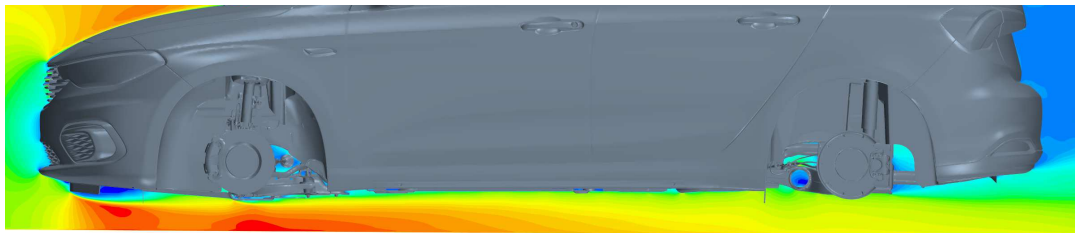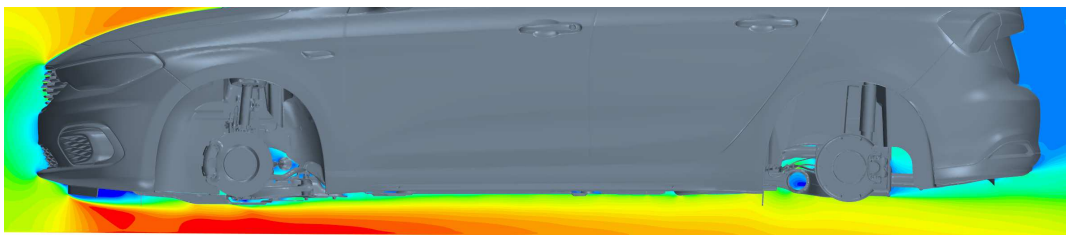
FIGURE 4.34: Engine shields comparisons.

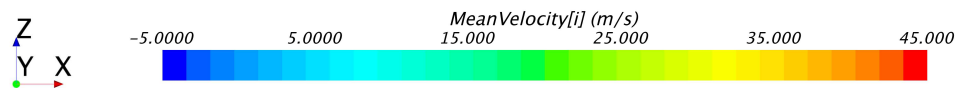(A) *NP-conf.*

(B) *2nd-conf.*

(C) *3rd-conf.*

FIGURE 4.35: Velocity-x distribution in the xz plane at $y = -0.3\ m$ for the three different engine shields configurations and SM model.
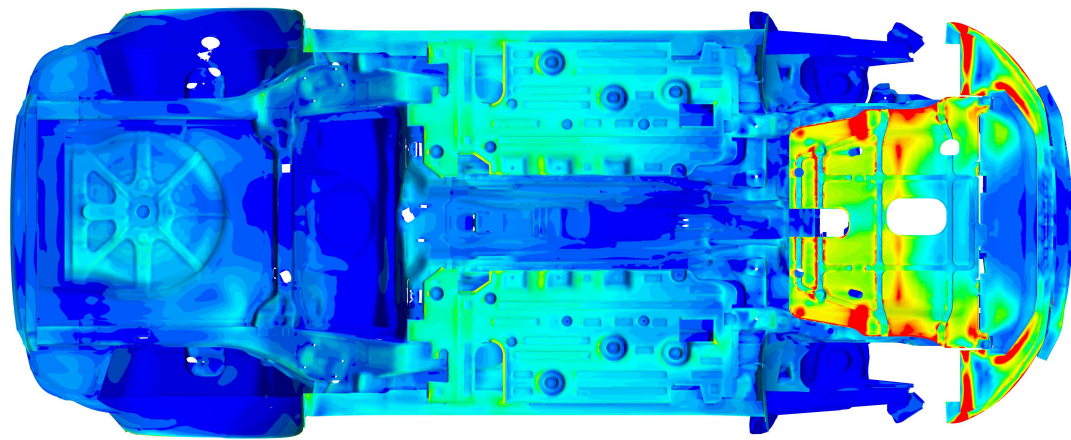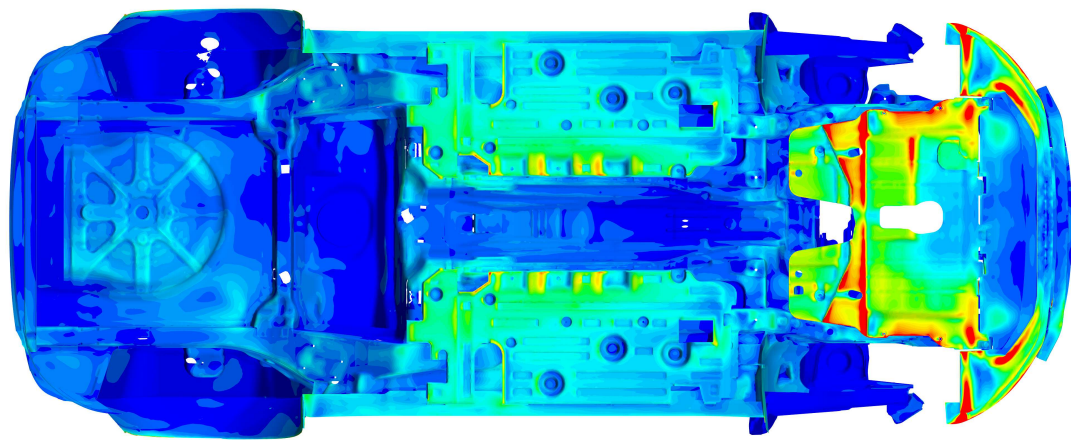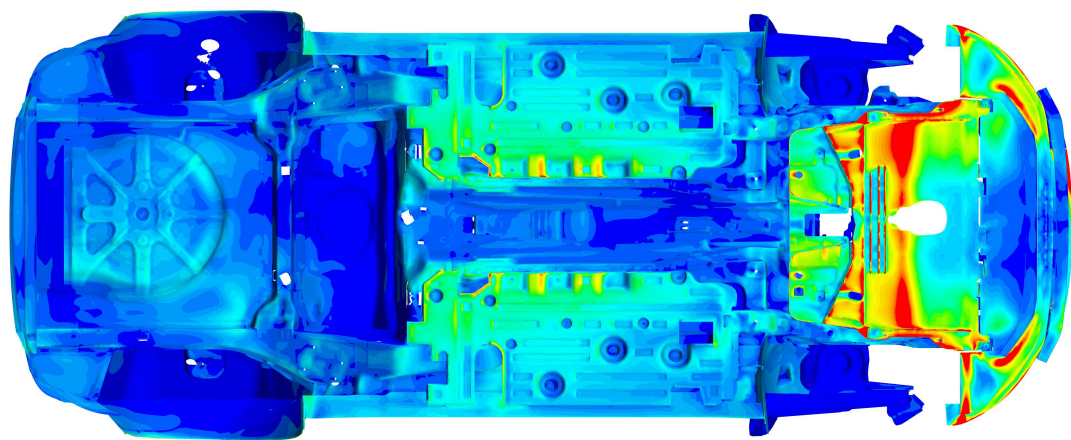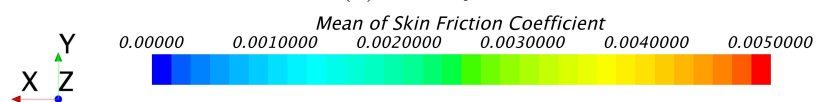
(A) *NP-conf.*

(B) *2nd-conf.*

(C) *3rd-conf.*

FIGURE 4.36: Underbody Skin Friction distribution for the three different engine shields configurations and SM model.

Conclusion

The purpose of this thesis was the investigation of different approaches in wheel rotation simulation, i.e. MRF, sliding mesh and overset, in order to better correlate CFD results with experimental ones. To this aim, different car configurations have been used.

In NP configuration, the best correlation, for total drag coefficient, is found with the MRF methodology. In fact, the error obtained with this method is about 1.9 %. Errors when using sliding mesh and overset are respectively of 9.8 % and 8.3 %.

These numbers suggest that a steady simulation and MRF model for the determination of the global coefficient drag are sufficient but, in order to find the best correlation for each different aerodynamic enabler, different configurations have been tested (each of them having a different set of aerodynamic enablers). By the results, shown in Table 4.1, we can notice that a steady simulation with MRF methodology was not the best solution and, hence, two other different approaches have been adopted.

Looking to the histogram in Figure 4.37, in which numerical and experimental values of coefficients drag for the different car configurations and the different rotation wheel models are compared, we can conclude that the sliding mesh methodology is the one that provides a better correlation of the CFD result with the experimental ones, having a percentage error less than 1 %.

The same comparison has been made for three different engine shields configuration in which the overset model has been used. Results show that with the overset model the numerical approximation is the worst compared to MRF and SM cases even though it is the case that simulates the reality in the better way. For this cases, hence, we can say that MRF model is the one providing the better solution for *NP-conf.* and *3rd-conf.*
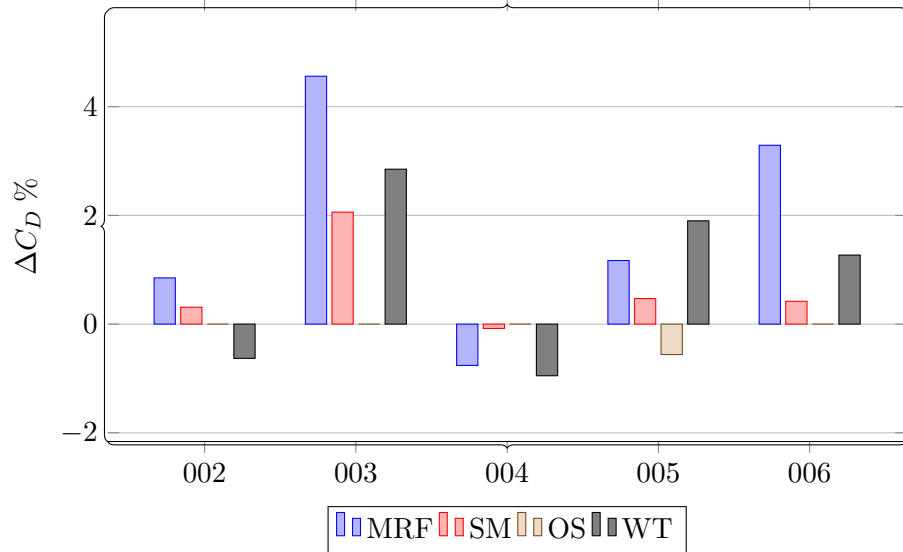
FIGURE 4.37: Results comparisons.

while for the *2nd-conf.* the error made is more than 2 % and the better model is the sliding mesh.

By looking at the accuracy with which the three methodologies approximate the flow features, we see that overset model better represents flow features since the rotation of the wheel has been implemented and an unsteady turbulent model has been used.

Concluding, what has emerged from this study is:

- MRF methodology provides, except for one aerodynamic enabler, a good correlation with experimental results in an acceptable run time but has the worst representation of the flow features;

- SM methodology produces a slight improvement in the correlation of aerodynamic enablers contributions and in flow features representation but requires a very long run time;

- OS methodology is the one giving the best representation of flow features and the worst numerical correlation of aerodynamic enablers contributions in a run time which is extremely long to be implemented for the standard of automotive companies.

A further development, aimed at completing the overview of the different methodologies to simulate wheel rotation, could be a simulation using the MRF methodology where the DES turbulent model is applied.

Bibliography

[1] Joseph Katz. *Automotive Aerodynamics*. Wiley, 2016.

[2] H K Versteeg W Malalasekera. *An Introduction to Computational Fluid Dynamics*. Pearson Prentice Hall, Second Edition.

[3] C. Hoever W. Kropp. A model for investigating the influence of road surface texture and tyre tread pattern on rolling resistance. *Journal of Sound and Vibration*, (351): 161–176, March 2015.

[4] T. Lajos T. Regert. Investigation of flow field past rotating wheels of cars. *The 12th International Conference on Fluid Flow Technologies*, Budapest, Hungary, September 3 - 6 2003.

[5] W.H. Hucho. Aerodynamics of road vehicles. 1993.

[6] P Lesniewicz et al. Aerodynamic analysis of an isolated vehicle wheel. *J. Phys.: Conf. Ser. 530 012064*, 2014.

[7] J.E. Fackrell J. K. Harvey. The aerodynamics of an isolate road wheel. *2nd AIAA symp. of aerodynamics of sports and competition automobiles*, 16:119–25, May 1974.

[8] M. Perić J.H. Ferziger. *Computational Methods for Fluid Dynamics*. 3rd Edition.

[9] Roberto Verzicco. Appunti di turbolenza. 2006-2007.

[10] Stephen B.Pope. *Turbolent Flows*. Cambridge University Press.

[11] *STAR-CCM + Documentation*. CD-adapco, Version 10.06.

Ringraziamenti

Desidero ringraziare tutti coloro che in questi mesi mi sono stati di aiuto e di supporto nella stesura.

Ringrazio anzitutto l'Ing. Laura Lorefice per avermi offerto la possibilità di effettuare la mia tesi presso il dipartimento di aerodinamica computazionale di FCA e che quindi mi ha permesso un arricchimento sia tecnico che personale. Un ringraziamento non può che andare a Luca Miretti e Nicola Paola che in questi mesi sono stati di supporto grazie ai loro aiuti e consigli. Ringrazio tutti i ragazzi dell'ufficio che in un modo o nell'altro hanno contribuito alla mia crescita professionale.

Vorrei ringraziare i miei relatori, i professori Iuso G. e D'Ambrosio D. per il loro preziosi consigli e per avermi fornito tutti gli strumenti necessari per portare a compimento la mia tesi.

In questi anni un ruolo importare lo hanno ricoperto i miei amici (Piero, Leonardo, Domenico, Ornella, Arianna, Valerio, Matteo, Marco, Vincenzo e Nazareno, spero di non aver dimenticato nessuno) ragazzi eccezionali che hanno reso questi anni più piacevoli. Per il suo egocentrismo merita di essere citato a parte il mio amico Madalin che con il suo atteggiamento spavaldo ma a volte anche sensibile non è mancato mai di una parola di conforto o di incitamento.

In questi anni a Torino ho conosciuto una persona fantastica che fin dal primo giorno di conoscenza mi ha dimostrato il suo grande affetto, la mia ragazza Simona. In questi anni è stato un punto fermo su cui poter fare affidamento e che ha rappresentato la mia famiglia con cui condividere la quotidianità.

Un ringraziamento a Lucia che nei primi anni di permanenza a Torino mi ha aiutato ad ambientarmi, offrendomi ospitalità e aiuto.

Vorrei ringraziare i miei genitori per il sostegno economico ma soprattutto morale e per non smettere mai di credere in me. Infine ci sono i miei fratelli Andrea e Silvia, oltre che semplici fratelli sono due persone su cui poter far affidamento, sempre disponibili a fornire consigli e aiuto qualora ce ne sia bisogno.

Grazie a tutti!